

## Supporting Information

### **Overall design of novel 3D-ordered MEA with drastically enhanced mass transport for alkaline electrolyzers**

*Lei Wan, Ziang Xu, Qin Xu, Peican Wang and Baoguo Wang\**

The State Key Laboratory of Chemical Engineering, Department of Chemical Engineering, Tsinghua University, Beijing  
100084, People's Republic of China

\*Email: [bgwang@tsinghua.edu.cn](mailto:bgwang@tsinghua.edu.cn) (Baoguo Wang)

## Experimental Section

### Materials

Aluminum foil (AF) (99.99%), nickel foil (99.99%) and nickel foam were purchased from Tianjin Yiweixin Science and Technology Chemical Limited Corporation. Cobalt(II) chloride ( $\text{CoCl}_2$ , 99%), vanadium(III) chloride ( $\text{VCl}_3$ , 99%), ammonium chloride ( $\text{NH}_4\text{Cl}$ ), hydrochloric acid ( $\text{HCl}$ ), potassium hydroxide ( $\text{KOH}$ ) and N-methyl pyrrolidone (NMP, 99.99%) were purchased from Sigma Aldrich. p-Terphenyl (TP), biphenyl (BP), 1,2-diphenylethane (DP), 1-methyl-4-piperidone, 9,9-dimethylfluorene, trifluoromethanesulfonic (TFSA), trifluoroacetic acid (TFA) and iodomethane were purchased from energy-chemical Co. Ltd (China). Carbon rod and Pt foil electrodes were obtained from Tianjin Aida Heng Sheng Technology Development Co. LTD. All the chemical agents were analytical grade.

### Methods

#### Preparation of self-supported porous VCoP nanoarrays

The self-supported porous VCoP nanoarrays were firstly electrodeposited at different current densities (100, 500, 1000 and 2000  $\text{mA cm}^{-2}$ ) for 90 s at 25 °C using an electrochemical workstation through a two-electrode system. AF of  $2 \times 3 \text{ cm}^2$  was used as the cathode electrode. The Pt foil of  $1 \times 1 \text{ cm}^2$  was used as anode electrode. The bath solution was composed of 0.1 M  $\text{CoCl}_2$ , 0.1 M  $\text{VCl}_3$ , 0.5 M  $\text{NaH}_2\text{PO}_2 \cdot \text{H}_2\text{O}$  and 1 M  $\text{NH}_4\text{Cl}$ . The as-prepared self-supported VCoP/AF sample was washed with ethanol and deionized (DI) water prior to drying in a vacuum oven at 50 °C, for 1 h. The self-supported VCoP/nickel foil sample was prepared by substituting AF as nickel foil *via* the same process. The electrodeposited catalysts loading to be  $\sim 2.0 \text{ mg cm}^{-2}$ .

## Preparation of alkaline resistant polymers

PBI was synthesized following our work reported previously<sup>1</sup>. PPA (153 g) was heated to 150 °C in a three-necked flask, which equipped with a mechanical stirring and N<sub>2</sub> atmosphere. DAB (3.2427 g) was added into the three-necked flask, and mechanical stirred at 150 °C for 3 h. Then the temperature was heated up to 200 °C, following triphenyl phosphate (0.065 g) and P<sub>2</sub>O<sub>5</sub> (4.5 g) were poured into the three-necked flask in sequence and reacted for 24 h. After polymerization reaction, the obtained polymers were further purified by the treatments of NaHCO<sub>3</sub> and DI.

The poly(alkyl-terphenyl piperidinium) polymers were synthesized following recently reported literature<sup>2</sup>. TP (3.885 g), DP (1.0252 g) and MP (2.8005 g) were added to a 200 mL double-jacketed glass reactor with a mechanical stirrer. After that, 18 mL of CH<sub>2</sub>Cl<sub>2</sub> was added into the reactor as a solvent. When the setting temperature was below 3 °C, TFA (2.7 mL) and TFSA (18 mL) were slowly added to the solution, and the reaction proceeded at 1 °C for ~12 h. The color of the solution changed from yellow-green to dark green. Finally, the viscous solution was poured into 1 L DI water to precipitate the polymer. Subsequently, the large polymer fiber was cut into small pieces by using a blender. Then, it was washed with DI water 4 times until neutral pH. The polymer was dried in an oven at 70 °C for 24 h to obtain flavescent poly(diphenyl-co-terphenyl N-methyl piperidine) (PDTM). Then PDTM (6.0 g) was dissolved in DMSO (100 mL) in a 250 mL single-neck flask with a magnetic stirrer. Subsequently, K<sub>2</sub>CO<sub>3</sub> (3.6 g) and iodomethane (5.5 g) were added into the polymer solution, and the reaction proceeded at room temperature under magnetic stirring for 24 h in a dark environment. The polymer solution was precipitated in 800 mL of ethyl acetate and was washed with DI water

several times to remove remaining iodomethane and salt. Finally, the polymer was dried in an oven at 60 °C for overnight to obtain a light-yellow poly(diphenyl-co-terphenyl dimethyl piperidinium) powder.

### **Preparation of novel 3D-ordered membrane electrode assembly**

Conventionally, the polymer membranes are typically cast from a polymer solution, and then following solvent evaporation. However, to prepare the novel 3D-ordered MEAs in this work, a novel direct membrane deposition technique is utilized. The as-prepared self-supported VCoP/AF electrode was employed as bifunctional electrode. The polybenzimidazole (PBI) polymer dispersion is directly deposited on top of two as-prepared self-supported VCoP/AF electrodes via an ultrasonic spray setup. For PBI polymer dispersion fabrication, PBI polymer (1 g) is dissolved in ethanol (99 g) to form uniform solution. In addition, for poly (diphenyl-co-terphenyl dimethyl piperidinium) dispersion fabrication, poly(diphenyl-co-terphenyl dimethyl piperidinium) polymer (1 g) is dissolved in DMSO (99 g). The MEA for AEMWE is constructed by assembling the membrane-coated self-supported VCoP/AF electrodes with the membrane layers facing each other before membrane solidification. Then as-prepared MEA was dried in a vacuum oven at 50 °C, for overnight. To etch the AF forming porous gas diffusion layer, the as-prepared MEA was immersed into 1 M KOH solution at room temperature for 12 h.

### **Preparation of conventional 3D-ordered membrane electrode assembly**

To prepare the conventional 3D-ordered MEA, the highly porous VCoP-2 foams were decaled to the both sides of a self-supported membrane by hot pressing at a condition of 2 MPa and 140 °C for 5 min.

### **Preparation of conventional membrane electrode assembly**

The preparation methods of conventional MEAs include catalyst coated substrate (CCS) and catalyst coated membrane (CCM) techniques. The commercial noble-metal Pt/C and IrO<sub>2</sub> catalysts were employed as HER and OER catalysts, respectively. The catalyst powders were first ground in a mortar for uniformity. For the catalyst ink preparation, 5 mg of each electrocatalyst powders was mixed with 40 μL ionomer solution and 1 mL ethanol. The mixed solution was subjected to ultrasonication for 5 h to form a highly disperse catalyst ink. For the CCS method, the ink was immediately spray onto nickel foam. The loading mass of catalysts was about 2.0 mg cm<sup>-2</sup>. Subsequently, cathode and anode were sandwiched with a self-supported PBI membrane and hot-pressed at 120 °C for 2 min. For the CCM method, the ink was immediately spray onto both sides of a self-supported PBI or poly(alkyl-terphenyl piperidinium) membrane, respectively. The loading mass of catalysts was about 2.0 mg cm<sup>-2</sup>. Then, the cathode and anode nickel foam were sandwiched with the catalyst coated membrane and pressed to form MEA.

### **Materials Characterization**

The morphology of samples was characterized via transmission electron microscopy (TEM, FEI Tecnai Arctica) and scanning electron microscopy (SEM, Zeiss Merlin). X-ray diffraction (XRD) was carried out on a Bruker machine with Cu Kα ( $\lambda = 0.15418$  nm) as the source. The chemical composition was analyzed using X-ray photoelectron spectroscopy (XPS), which used a Kratos Axis Ultra DLD spectrometer employing a monochromated Al Kα X-ray source

( $h\nu = 1486.6$  eV). The structure of self-supported VCoP/AF electrodes was analyzed by means of a white light interferometry profiling system (WLI) (Bruker Contour GT K0 G, Germany). The completely contactless optical method is a type of microscope, in which white light from a source is split into two paths by a partially reflecting mirror called a beam splitter, left side. One path directs light to a flat from the two surfaces are recombined in the microscope and imaged at a digital camera. If the path difference between the recombined beams is in the order of a few wavelengths of light or less, interference occurs. These fringes correspond to the contour of the surface of the sample, mapping its vertical topography with a resolution as high as few nanometers. The contact angles (CA) and interface tension were measured by Contact Angle Tester (Data physics Co. Ltd., GER OCA-20). The adhesion strength of MEAs were measured by a peel-off test. The  $180^\circ$  peel-off strength was recorded 5 times for each sample by a universal testing machine at  $25^\circ\text{C}$ . To measure the hydrogen permeation of MEAs and membranes, the alkaline electrolyte or pure water was filled at  $30^\circ\text{C}$  on both sides of the cell, which comprised a MEA with an active area  $5\text{ cm}^2$ . The pressure difference was determined from 1.1 to 1.5 bar using a single stage backpressure regulator (44-2361-24, TESCO<sup>TM</sup>, Minneapolis, MN, USA) and mass flow controller (5850E, Brooks Instrument, Hatfield, PA, USA). The lower-side of pressure was referred to as the anode, while the higher-side was referred to as the cathode. When the electrolyte permeated the MEA, the change of mass was recorded. According to Darcy's law, the hydrogen permeation flux density ( in  $\Phi^{Dary}_{H_2}$  mol s<sup>-2</sup> cm<sup>-1</sup> bar<sup>-1</sup>) and hydrogen permeability ( $\varepsilon^{Dary}_{H_2}$  in mol s<sup>-1</sup> cm<sup>-1</sup> bar<sup>-1</sup>) are defined as:

$$\Phi^{Dary}_{H_2} = -\varepsilon^{Dary}_{H_2} (\Delta p/d)$$

$$\varepsilon^{Dary}_{H_2} = (KSp^{cat})/\eta$$

where  $\Delta p$  indicates the absolute pressure difference of the cell (bar);  $d$ , membrane's thickness (cm);  $S$ , hydrogen solubility ( $\text{mol m}^{-3} \text{ bar}^{-1}$ );  $\eta$ , viscosity (bar s);  $p^{\text{cat}}$ , hydrogen partial pressure on the cathode side (bar);  $K$ , electrolyte permeability ( $\text{cm}^2$ ).

## Electrochemical Measurements

Electrochemical measurements were performed to evaluate the activity and stability of as-prepared self-supported VCoP/NF electrode using a Princeton electrochemical workstation in a standard three-electrode cell. The self-supported VCoP/NF electrode with an exposed area of  $1 \text{ cm} \times 1 \text{ cm}$  was used as the working electrode. The carbon rod electrode and saturated calomel electrode (SCE) were used as counter electrode and reference electrode, respectively. The activities for OER and HER were evaluated by linear sweep voltammetry (LSV), Tafel and electrochemical impedance spectroscopy (EIS) in 1 M KOH at 30 °C. The LSV measurements were carried out at a scan rate of  $5 \text{ mV s}^{-1}$ . The Tafel slope was obtained from the polarization curve using a linear fitting. The stability of the self-supported VCoP/NF electrode for OER and HER were also evaluated using chronopotentiometry test at 100, 500 and 1000  $\text{mA cm}^{-2}$ , respectively. All electrochemical measurements were repeated at least twice under the same condition to ensure reproducibility and accuracy. All potentials were converted from the SCE to the reversible hydrogen electrode (RHE) according to equation (S1).

$$E_{\text{RHE}} = E_{\text{appl}} + E_{\text{SCE}} + 0.059 * pH = 1.05 \text{ V} + E_{\text{appl}} \quad (\text{S1})$$

## The performance test of MEAs

The flowing 1 M KOH solution was used as electrolyte and the temperature of cell can be

controlled at 20 °C to 60 °C by a constant temperature heating chamber. The potential range is from 1.2 V to 2.2 V at a scan rate of 1 mV s<sup>-1</sup>. The EIS measurements were carried out at 1.6 V<sub>cell</sub>. The frequency range was 10 kHz-0.01 Hz, and the amplitude was 5 mV. The complex nonlinear least square fitting of the impedance data was carried out with the Zview software. The corresponding energy conversion efficiency was calculated according to the following equations:

$$\eta = E_0/V \quad (\text{S2})$$

$$E_0 = -\Delta G/nF \quad (\text{S3})$$

$$\Delta G = \Delta H - T\Delta S \quad (\text{S4})$$

Where  $\eta$  is the energy conversion efficiency and  $E_0$  is the theoretical voltage of water electrolysis ( $\text{H}_2\text{O} \rightarrow \text{H}_2 + 1/2\text{O}_2$ ).  $n$  is the number of electrons,  $F$  is the Faradaic constant (96485 C mol<sup>-1</sup>),  $T$  is the reaction temperature and  $V$  is the measured voltage.  $\Delta G$  is the change of Gibbs free energy,  $\Delta H$  is the change of enthalpy (-285.8 kJ mol<sup>-1</sup>) and  $\Delta S$  is the change of entropy (-163.34 J K<sup>-1</sup> mol<sup>-1</sup>) during water electrolysis. To juxtaposes each corrected polarization curve by removing irreversible losses individually and sequentially, first, the  $iR$  drop (or ohmic overpotential,  $\eta_{\text{ohm}}$ ) is determined by the value of the x-intercept in the Nyquist plot from the EIS experiment, resulting in an  $iR$ -corrected voltage,  $E_{iR\text{-corrected}}$ .  $E_{\text{kin}}$  is then plotted using a linear approximation in the Tafel region (Tafel slope). The difference between  $E_{\text{kin}}$  and  $E_{iR\text{-corrected}}$  is thus equivalent to the mass transfer overvoltage. In order to analysis the purity of generated hydrogen gas, a systematic experiment was directly conducted to a gas chromatography instrument (490 Micro GC, Agilent, USA).



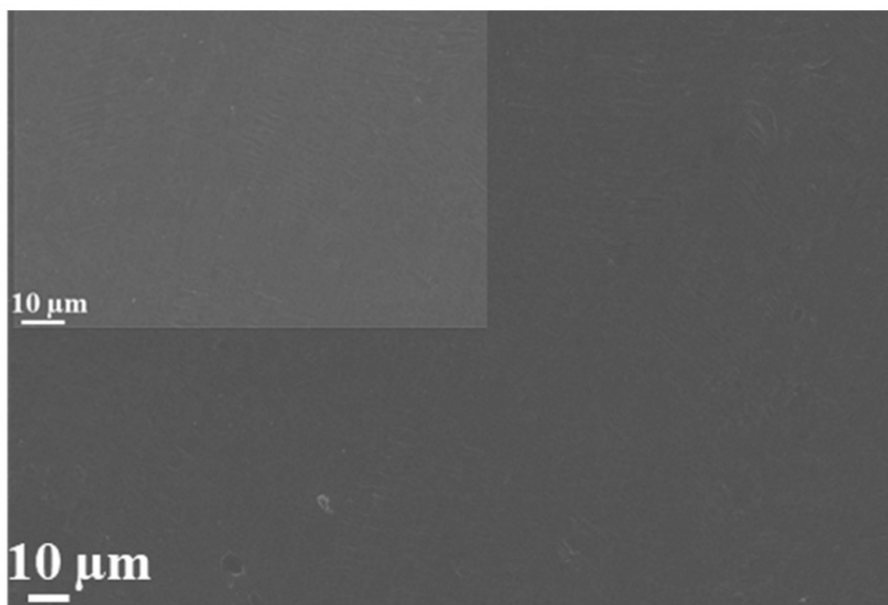


Figure S1. SEM images of Al foil (AF) as substrate for electrodepositing highly porous VCoP foams.

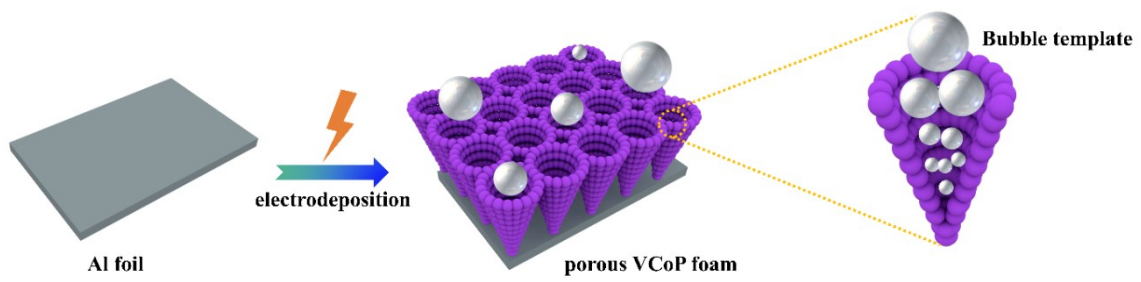


Figure S2. Schematic diagram of the synthetic route of porous VCoP foams by an electrodeposition method, in which the produced bubbles play the role as a template to fabricate vertical channels.

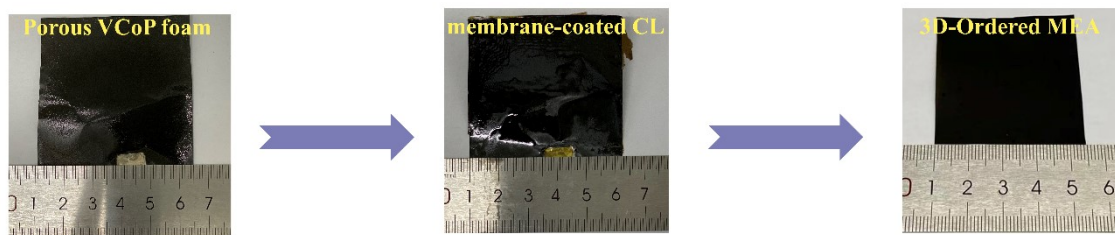


Figure S3. The photographic images of porous VCoP foam, membrane-coated catalyst layer and novel 3D-ordered MEA.

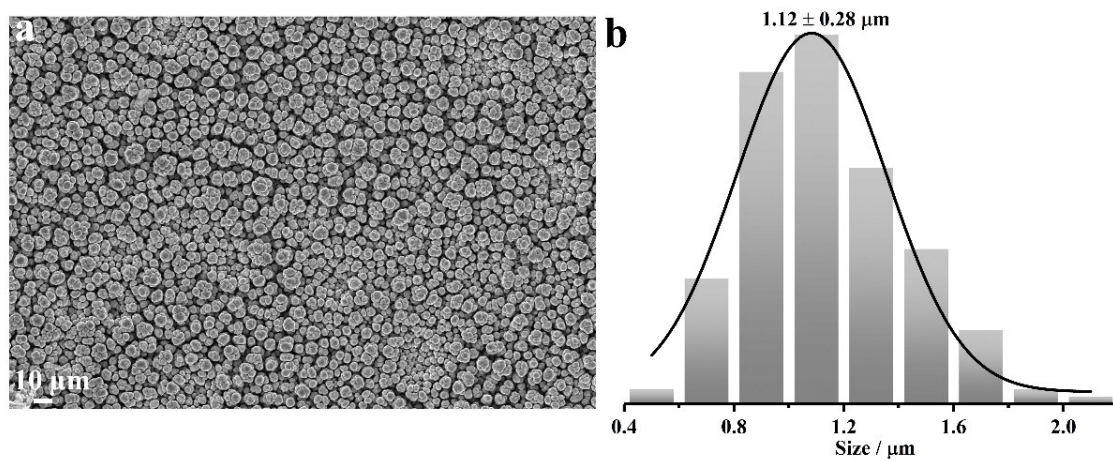


Figure S4. (a) SEM image of porous VCoP-0.1 foams at electrodeposition current density of  $0.1 \text{ A cm}^{-2}$ . (b) The histogram of cavity diameter distribution.

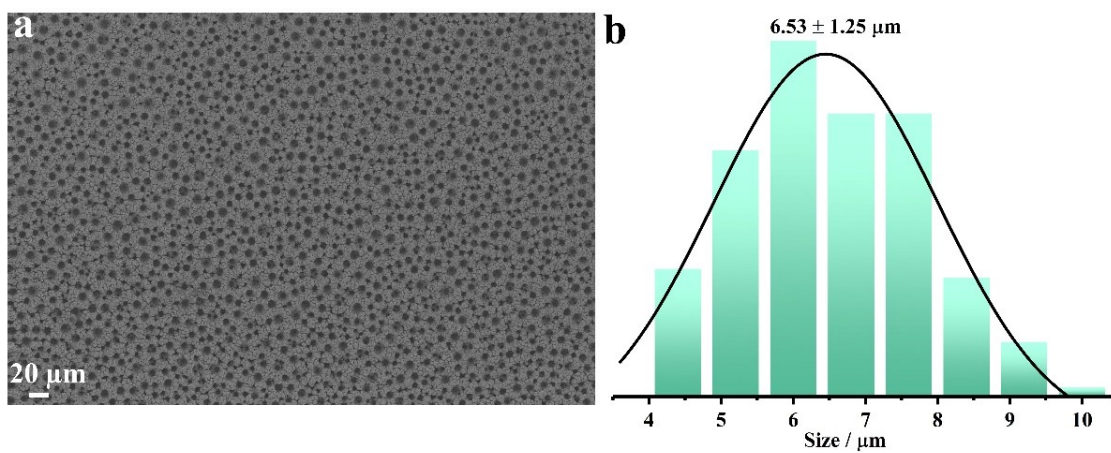


Figure S5. (a) SEM image of porous VCoP-0.5 foams at electrodeposition current density of  $0.5 \text{ A cm}^{-2}$ . (b) The histogram of cavity diameter distribution.

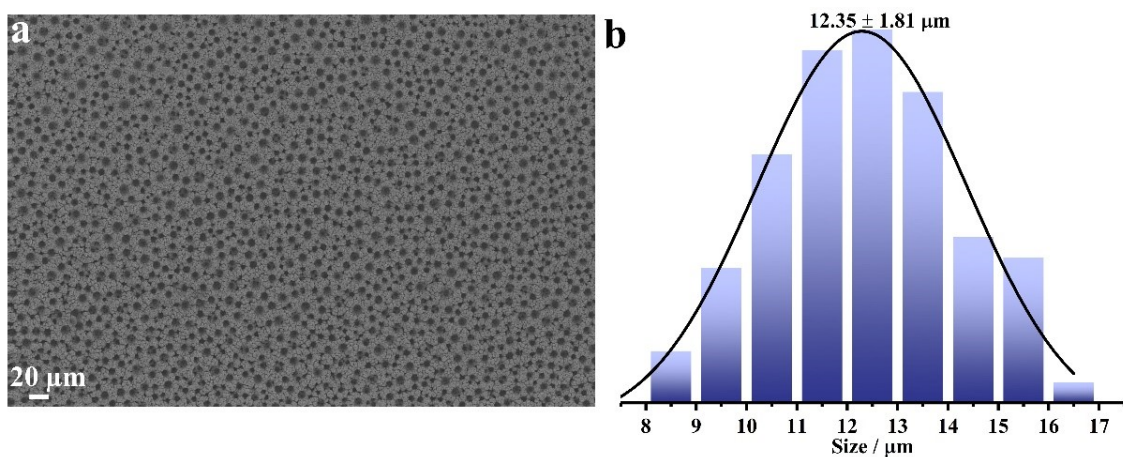


Figure S6. (a) SEM image of porous VCoP-1 foams at electrodeposition current of  $1 \text{ A cm}^{-2}$ .

(b) The histogram of cavity diameter distribution.

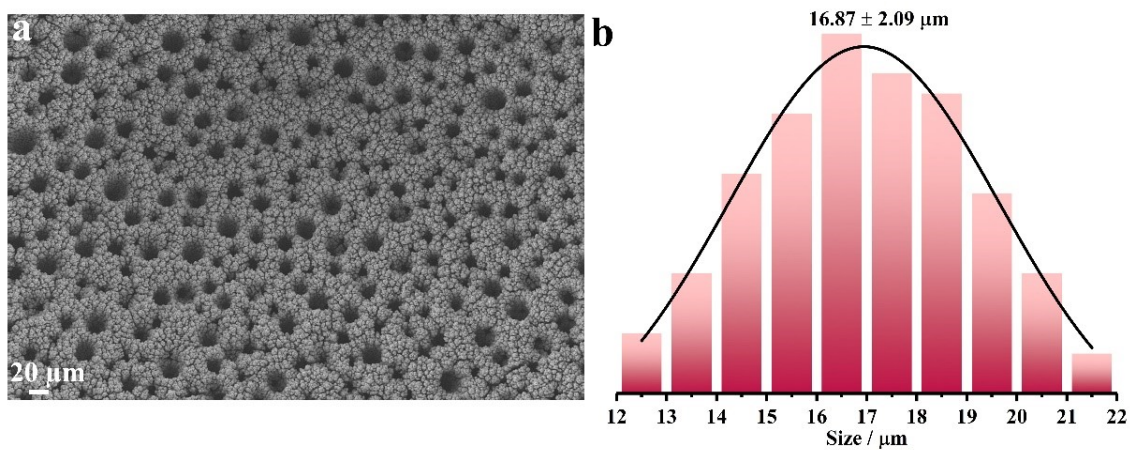


Figure S7. (a) SEM image of porous VCoP-2 foams at electrodeposition current density of 2 A cm<sup>-2</sup>. (b) The histogram of cavity diameter distribution.

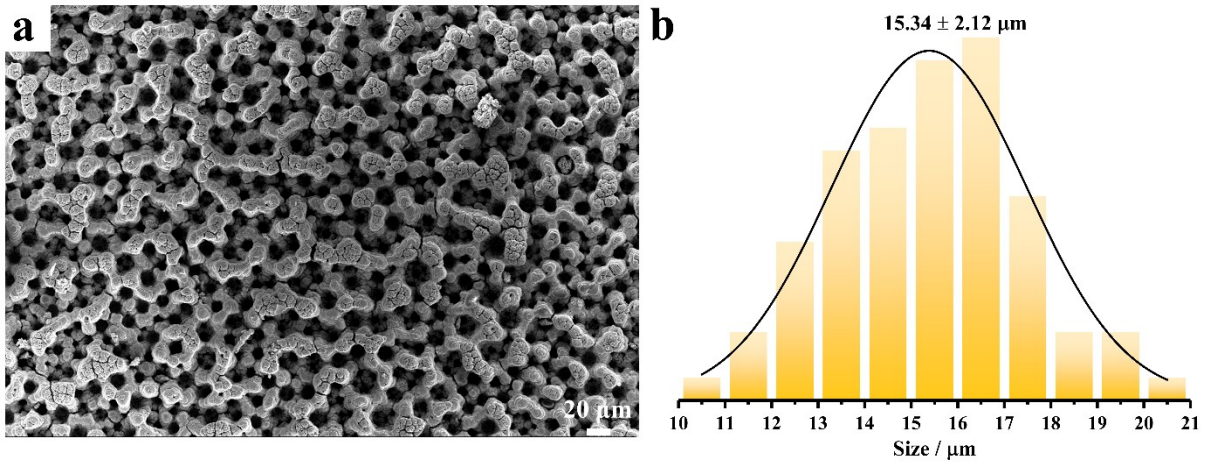


Figure S8. (a) SEM image of porous VCoP-3 foams at electrodeposition current density of 3 A cm<sup>-2</sup>. (b) The histogram of cavity diameter distribution.



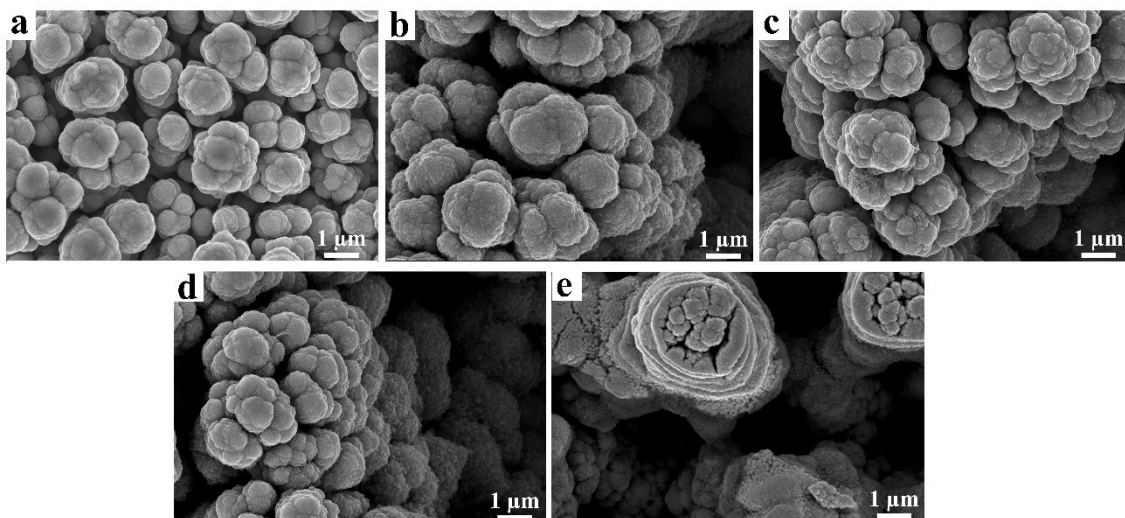


Figure S9. The high-resolution SEM images of (a) VCoP-0.1, (b) VCoP-0.5, (c) VCoP-1, (d) VCoP-2 and (e) VCoP-3.

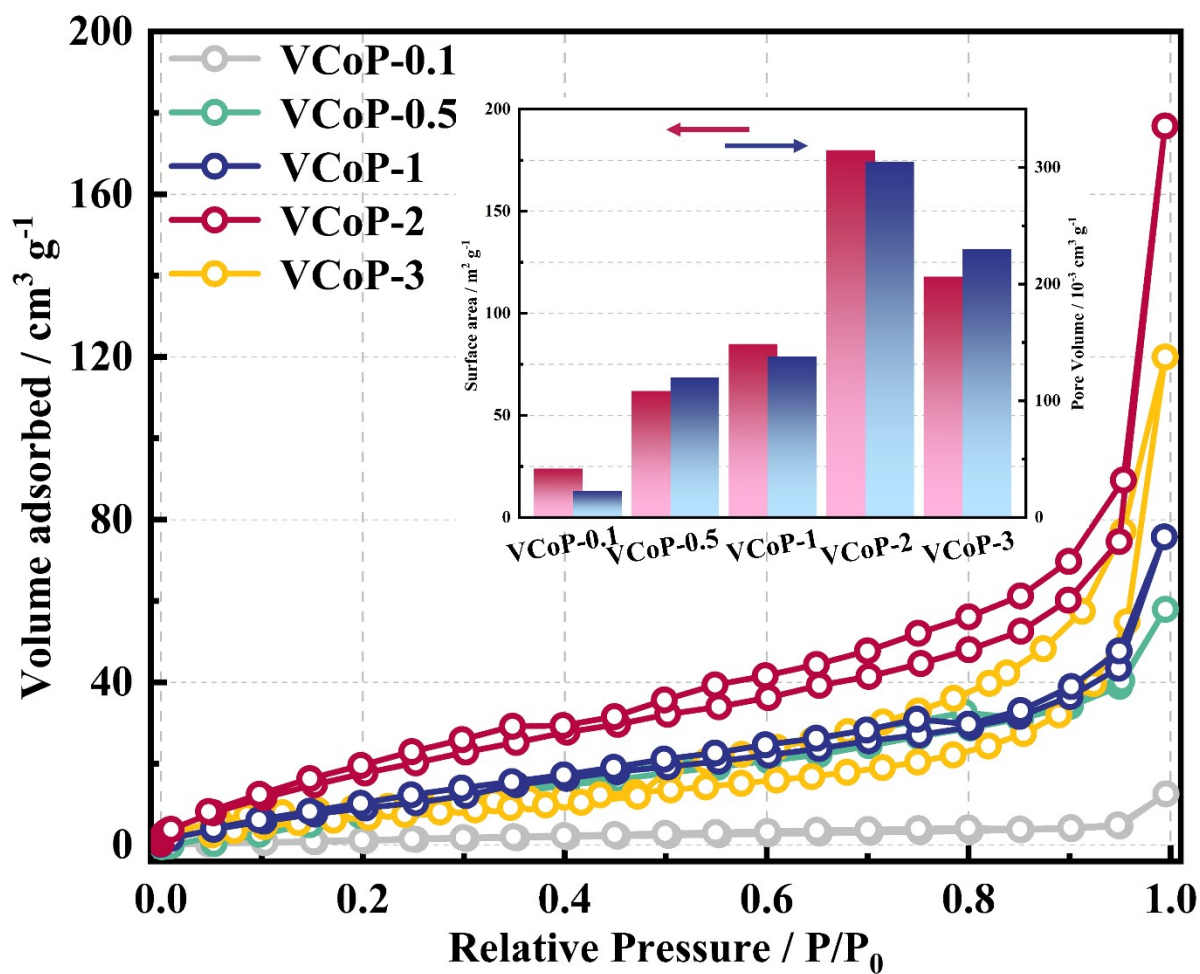


Figure S10. Nitrogen adsorption-desorption isotherms for the powder samples of VCoP prepared by different electrodeposition current densities, with a comparison of corresponding surface area and pore volume (inset).

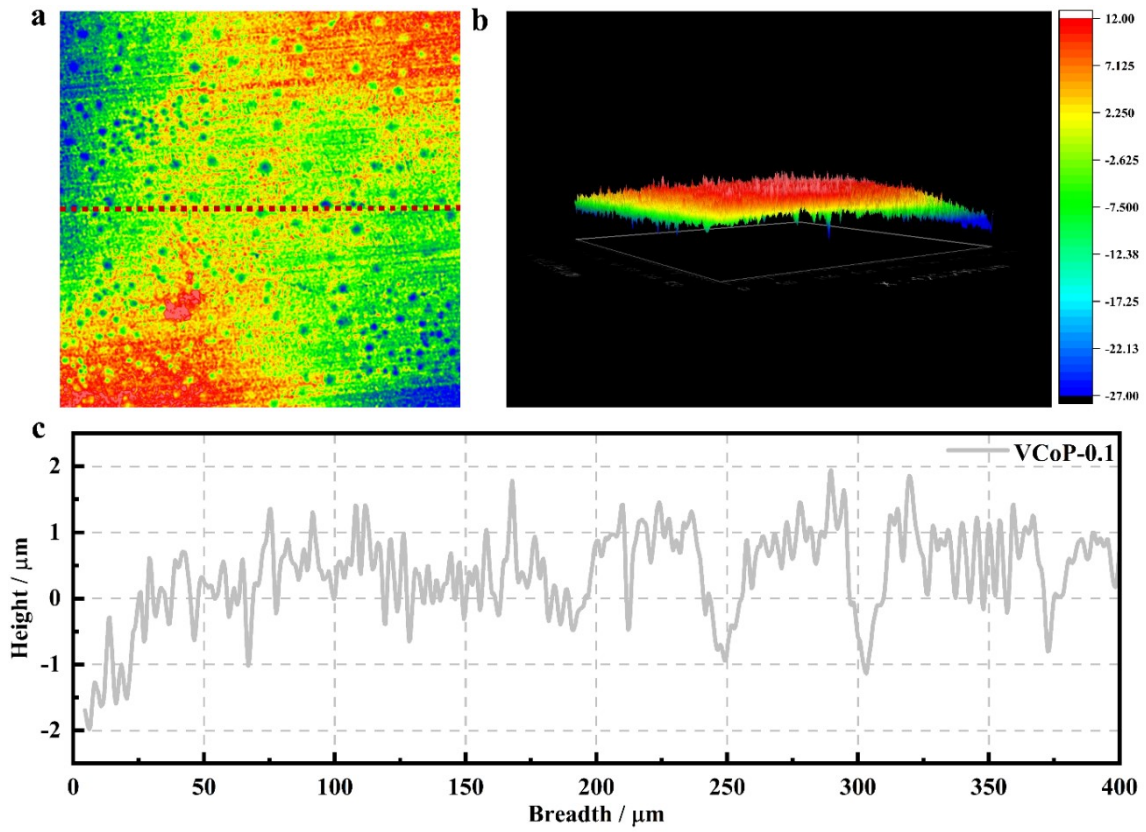


Figure S11. (a) 2D and (b) 3D WLI images of VCoP-0.1/AF (scan size =  $400 \times 400 \mu\text{m}$ ). A straight line cross the contact point is used to create a profile. (c) Line profile obtained along the red lines outlined in (a).

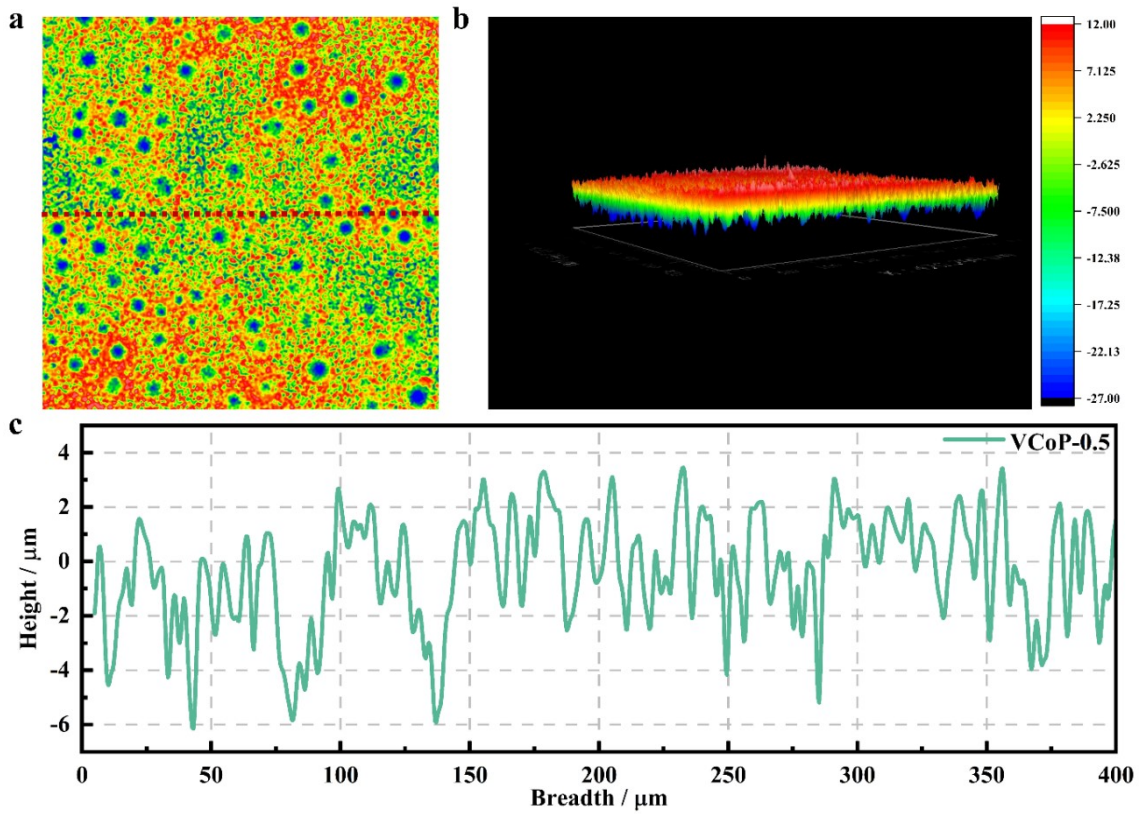


Figure S12. (a) 2D and (b) 3D WLI images of VCoP-0.5/AF (scan size =  $400 \times 400 \mu\text{m}$ ). A straight line cross the contact point is used to create a profile. (c) Line profile obtained along the red lines outlined in (a).

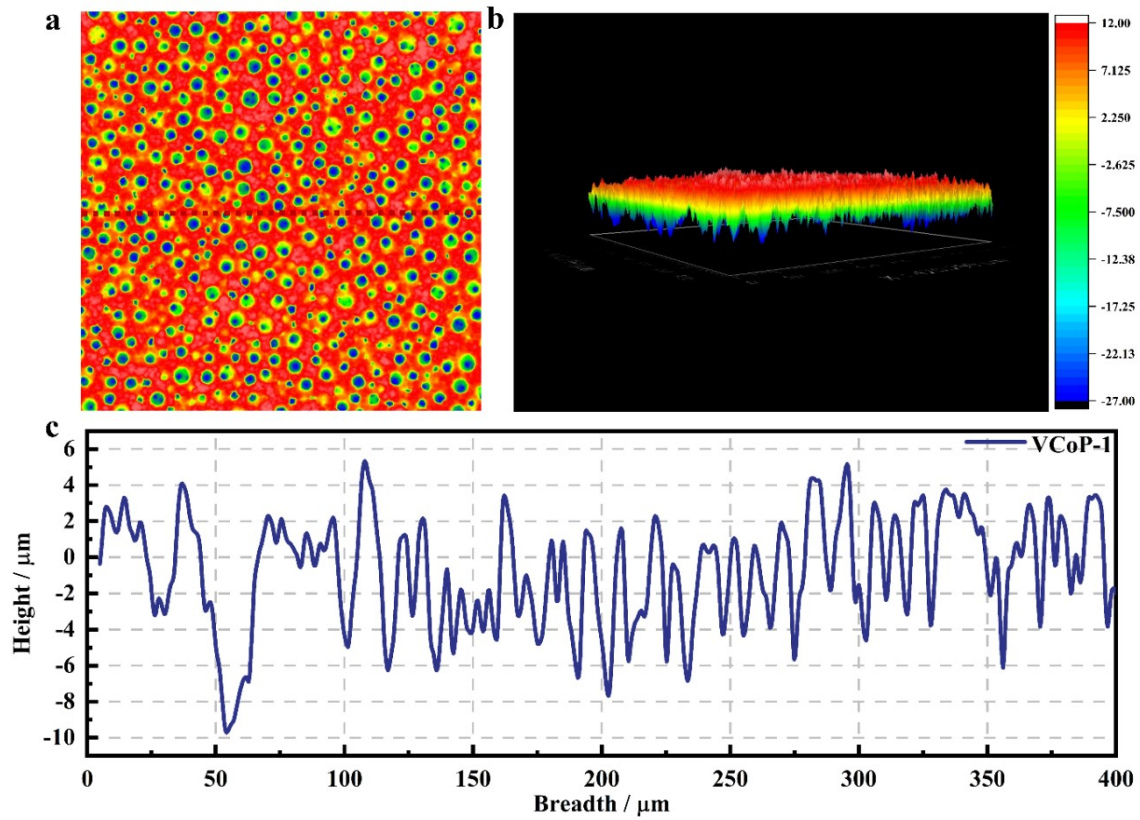


Figure S13. (a) 2D and (b) 3D WLI images of VCoP-1/AF (scan size =  $400 \times 400 \mu\text{m}$ ). A straight line cross the contact point is used to create a profile. (b) Line profile obtained along the red lines outlined in (a).

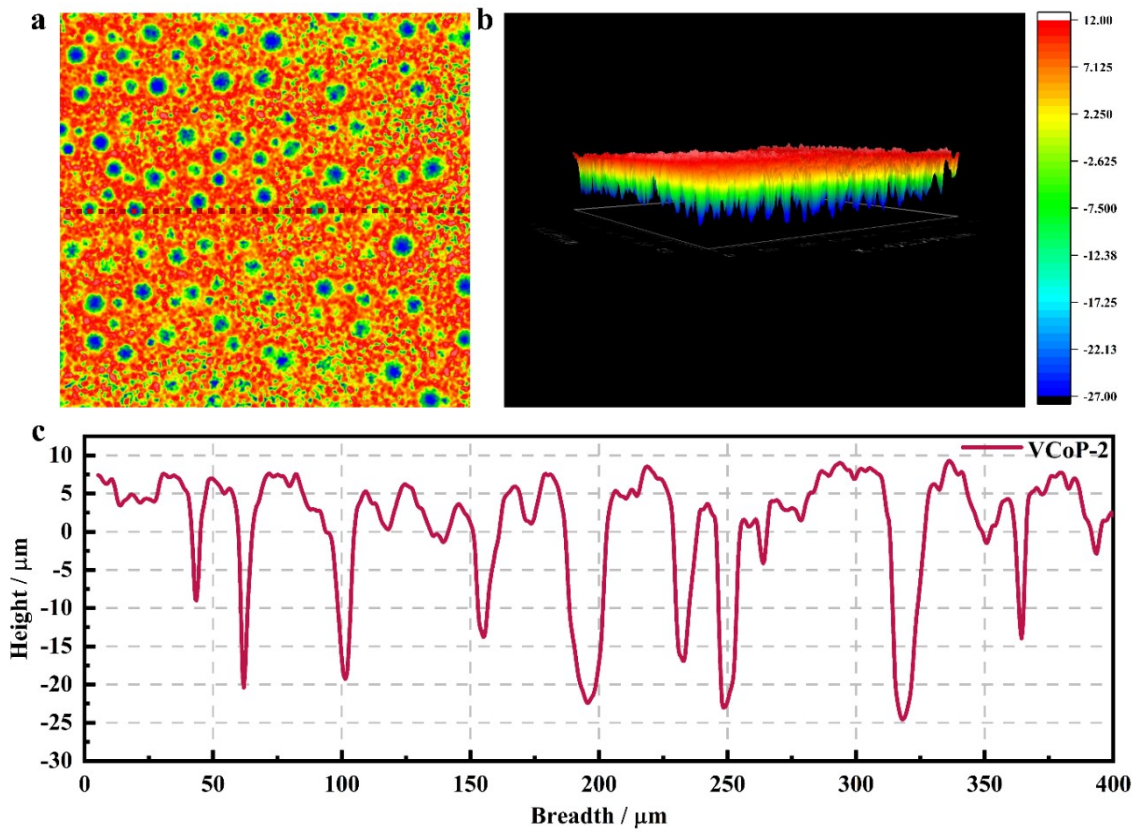


Figure S14. (a) 2D and (b) 3D WLI images of VCoP-2/AF (scan size =  $400 \times 400 \mu\text{m}$ ). A straight line cross the contact point is used to create a profile. (b) Line profile obtained along the red lines outlined in (a).

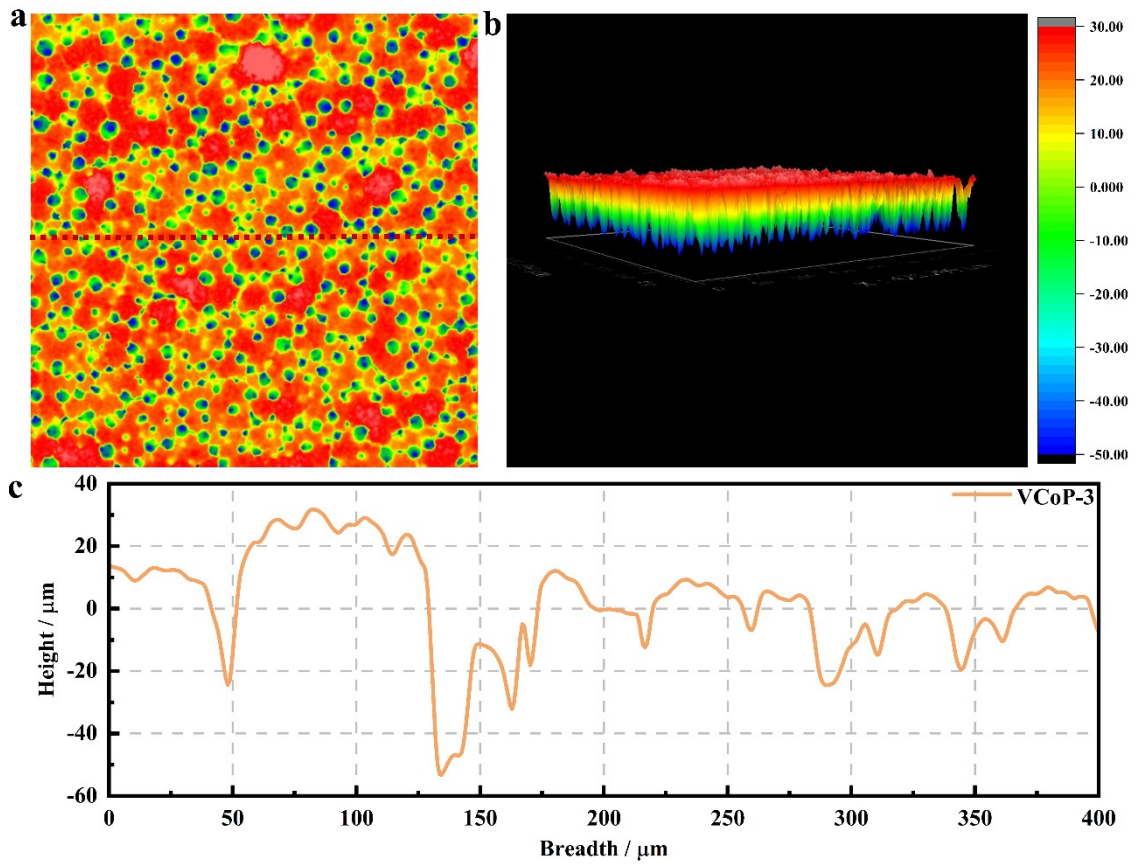


Figure S15. (a) 2D and (b) 3D WLI images of VCoP-3/AF (scan size =  $400 \times 400 \mu\text{m}$ ). A straight line cross the contact point is used to create a profile. (b) Line profile obtained along the red lines outlined in (a).

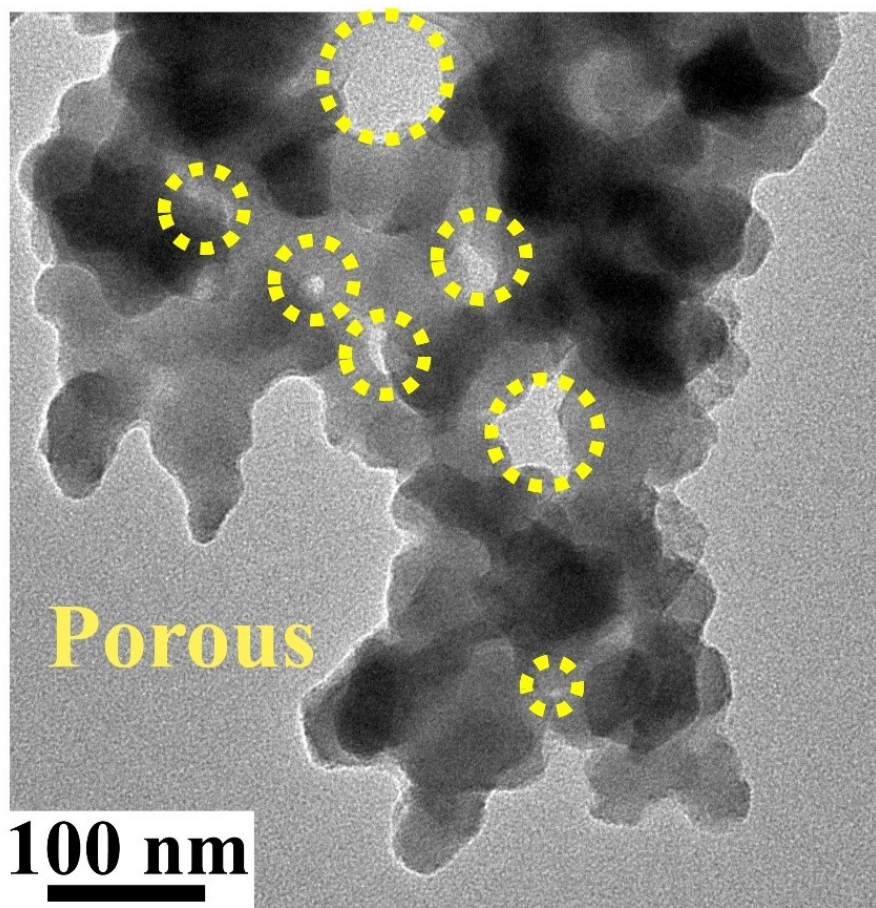


Figure S16. The TEM image of porous VCoP-2 foams.



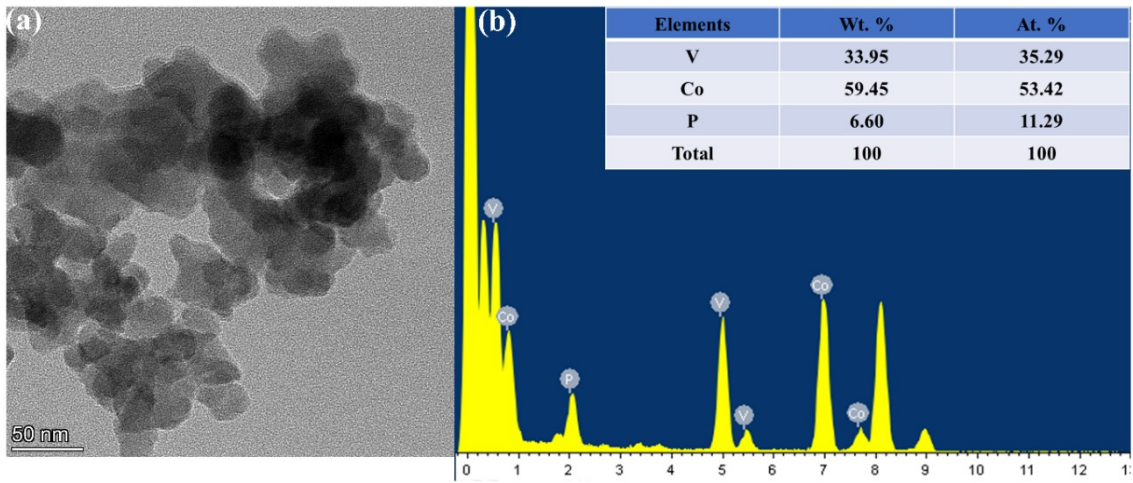


Figure S17. (a) TEM image of VCoP-2. (b) TEM-EDX spectra of VCoP-2.

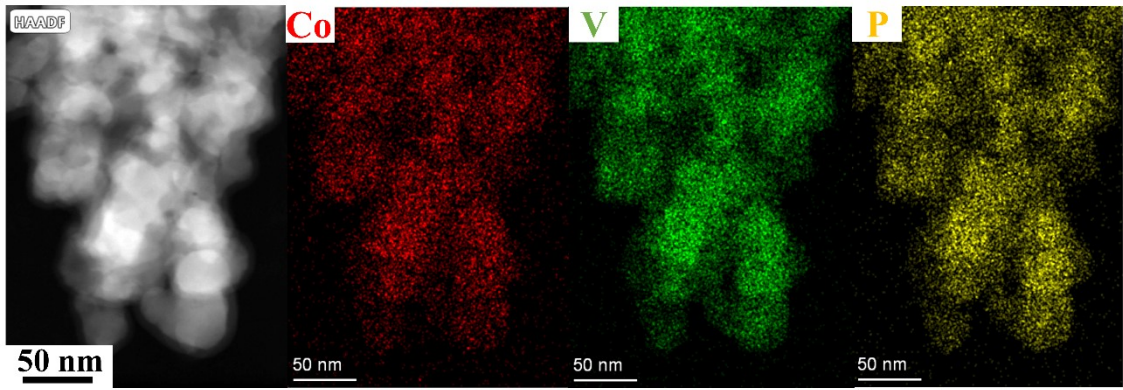


Figure S18. The TEM EDS mapping images of elemental Co, V and P in porous VCoP-2 foam.

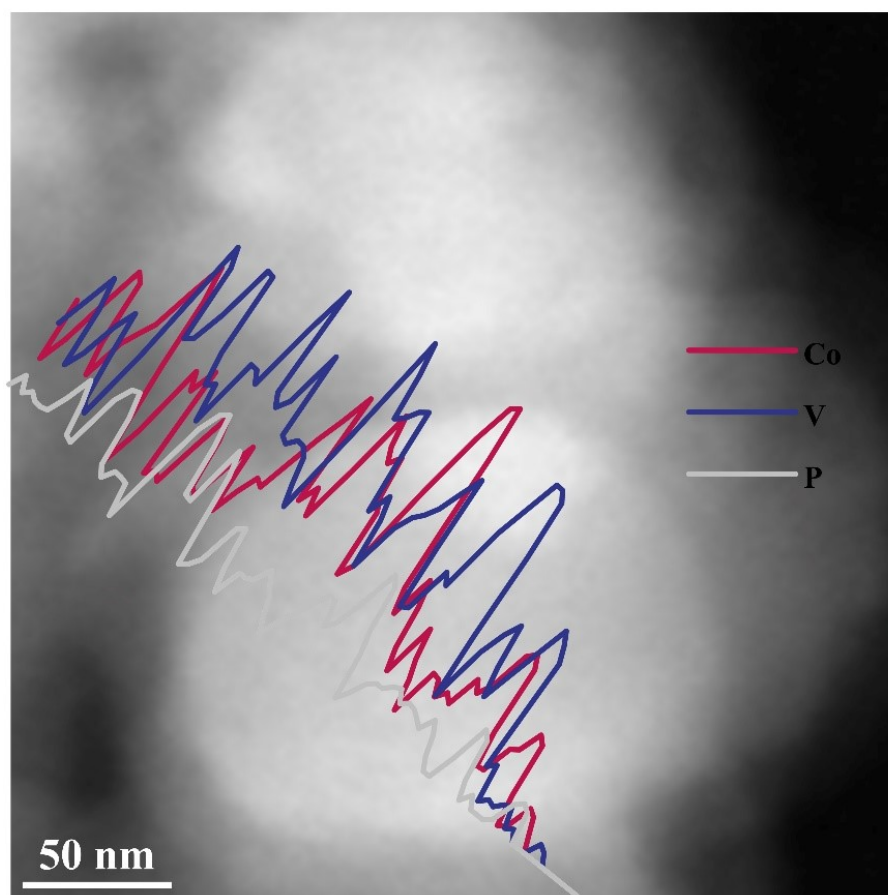


Figure S19. Line-scan analysis (inset) and HAADF-STEM image of VCoP-2.

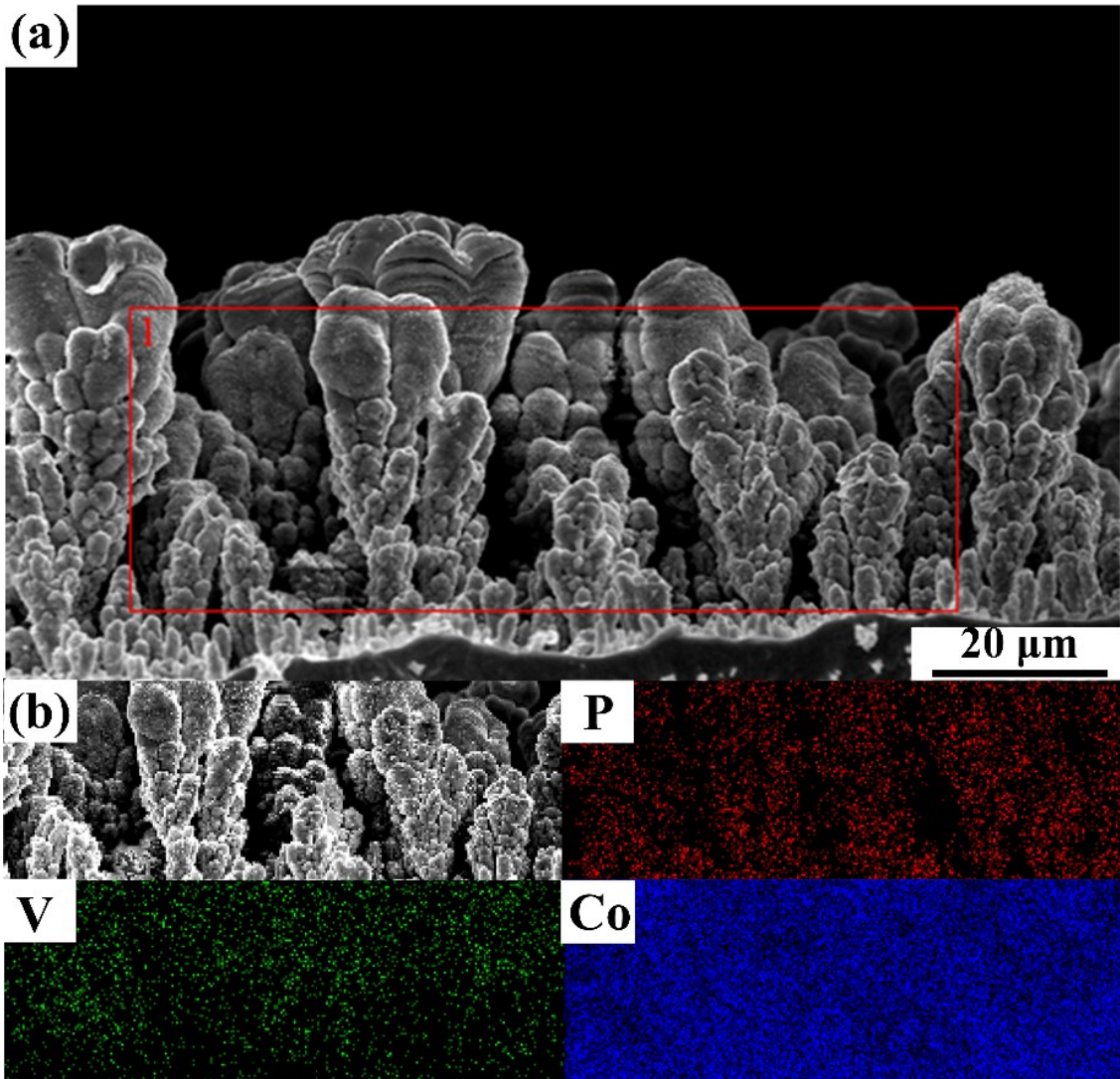


Figure S20. (a) Cross-section FE-SEM image of VCoP-2. (b) SEM elemental mappings of VCoP-2.

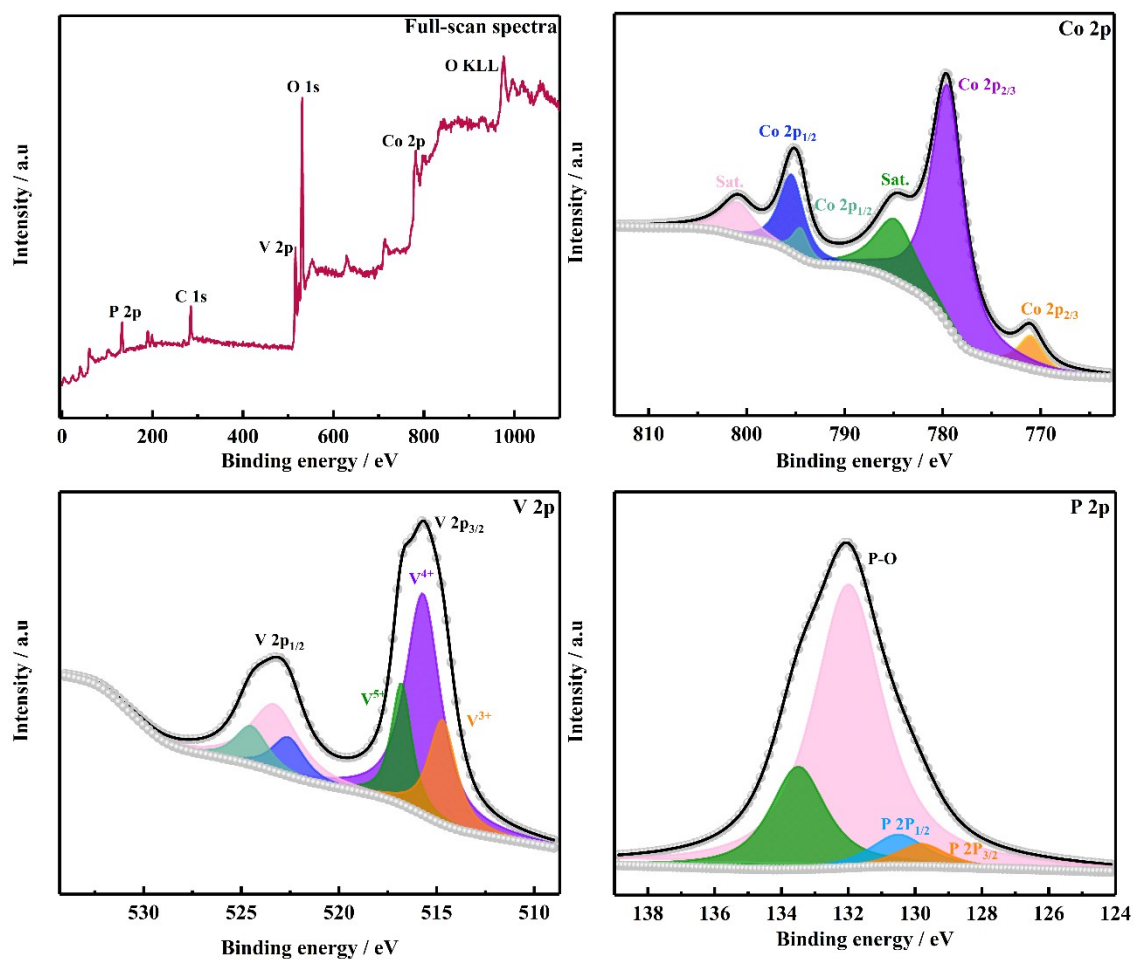


Figure S21. XPS spectra of porous VCoP-2 foam: (a) full-scan spectra, (b) Co 2p, (c) V 2p and (d) P 2p.

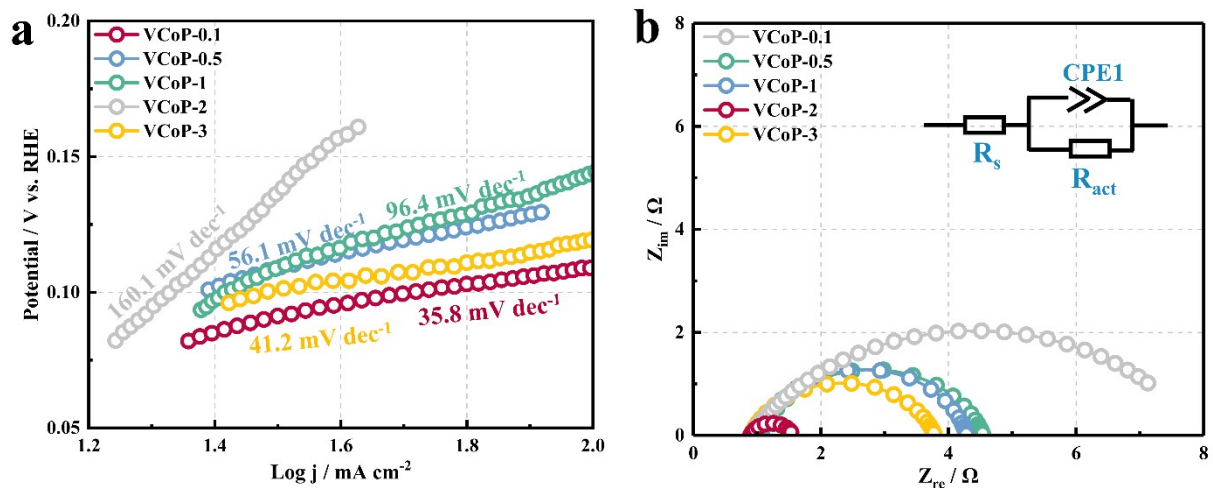


Figure S22. (a) Tafel plots and (b) EIS plots of VCoP/NF prepared by different electrodeposition current densities (100, 500, 1000, 2000 and 3000  $\text{mA cm}^{-2}$ ) for HER.

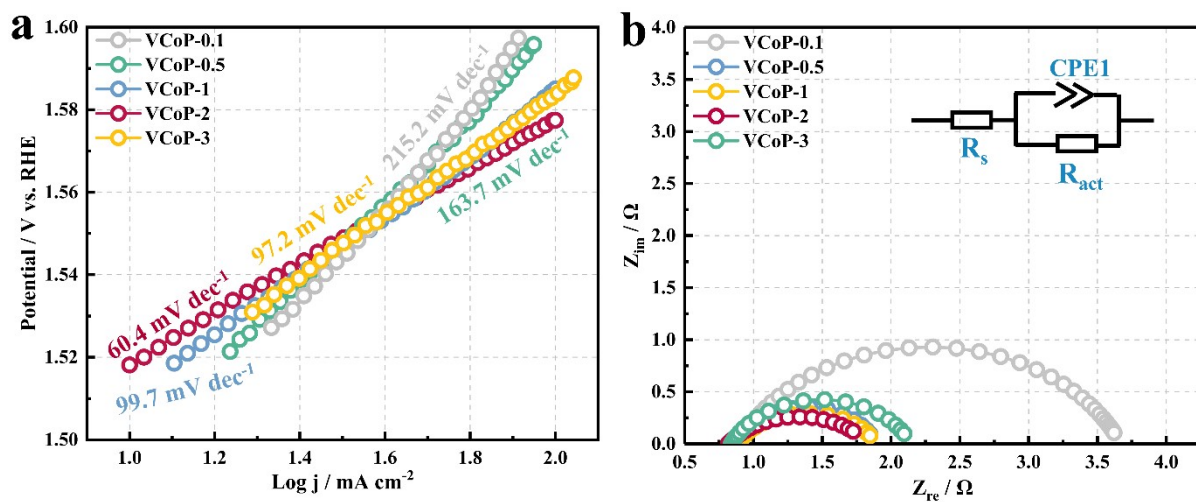


Figure S23. (a) Tafel plots and (b) EIS plots of VCoP/NF prepared by different electrodeposition current densities (100, 500, 1000, 2000 and 3000 mA cm<sup>-2</sup>) for OER.

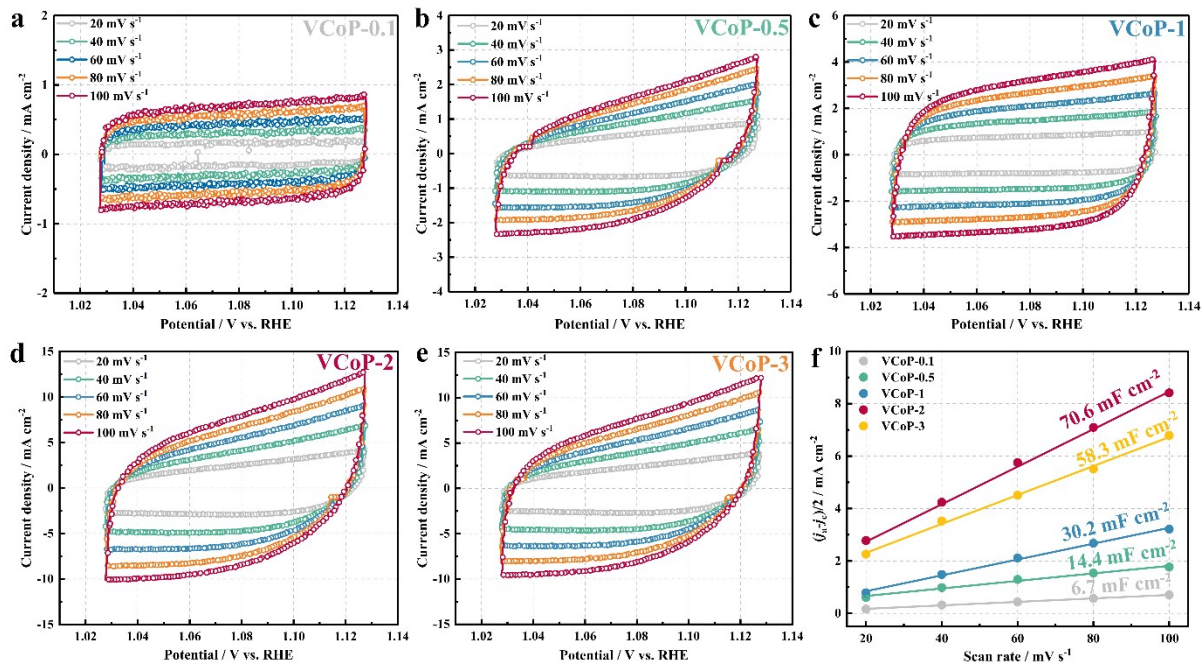


Figure S24. Capacitance study of the VCoP foams. (a) VCoP-0.1, (b) VCoP-0.5, (c) VCoP-1, (d) VCoP-2 and (e) VCoP-3 foams. The corresponding CVs measured at different scan rates from 20 to 100  $\text{mV s}^{-1}$  in potential region of 1.03~1.13 V (vs. RHE). (f) plots showing the extraction of  $C_{dl}$  for calculating ECSA. The plot of current density against scan rate has a linear relationship, and its slope is the double layer capacitance.

The specific capacitance can be converted into an electrochemical active surface area (ECSA) using the specific capacitance value for a flat standard with  $1 \text{ cm}^2$ . The ECSA is measured by the double-layer capacitance via CV curves in the double-layer region at different scan rates (Figure 13). The specific capacitance for a flat surface was generally found to be in the range of 20-60  $\mu\text{F cm}^{-2}$ . In the following calculations, we assumed it to be 40  $\mu\text{F cm}^{-2}$ .

VCoP-0.1:

$$A_{ECSA}^{VCoP-0.1} = \frac{6.7 \text{ mF cm}^{-2}}{40 \mu\text{F cm}^{-2} \text{ per cm}_{ECSA}^2} = 167.5 \text{ cm}_{ECSA}^2$$

VCoP-0.5:

$$A_{ECSA}^{VCoP-0.5} = \frac{14.4 \text{ mF cm}^{-2}}{40 \mu\text{F cm}^{-2} \text{ per cm}_{ECSA}^2} = 360.0 \text{ cm}_{ECSA}^2$$

VCoP-1:



$$A_{ECSA}^{VCoP-1} = \frac{30.2 \text{ mF cm}^{-2}}{40 \mu\text{F.cm}^{-2} \text{ per cm}_{ECSA}^2} = 755.0 \text{ cm}_{ECSA}^2$$

VCoP-2:

$$A_{ECSA}^{VCoP-2} = \frac{70.6 \text{ mF cm}^{-2}}{40 \mu\text{F.cm}^{-2} \text{ per cm}_{ECSA}^2} = 1765.0 \text{ cm}_{ECSA}^2$$

VCoP-3:

$$A_{ECSA}^{VCoP-3} = \frac{58.3 \text{ mF cm}^{-2}}{40 \mu\text{F.cm}^{-2} \text{ per cm}_{ECSA}^2} = 1457.5 \text{ cm}_{ECSA}^2$$

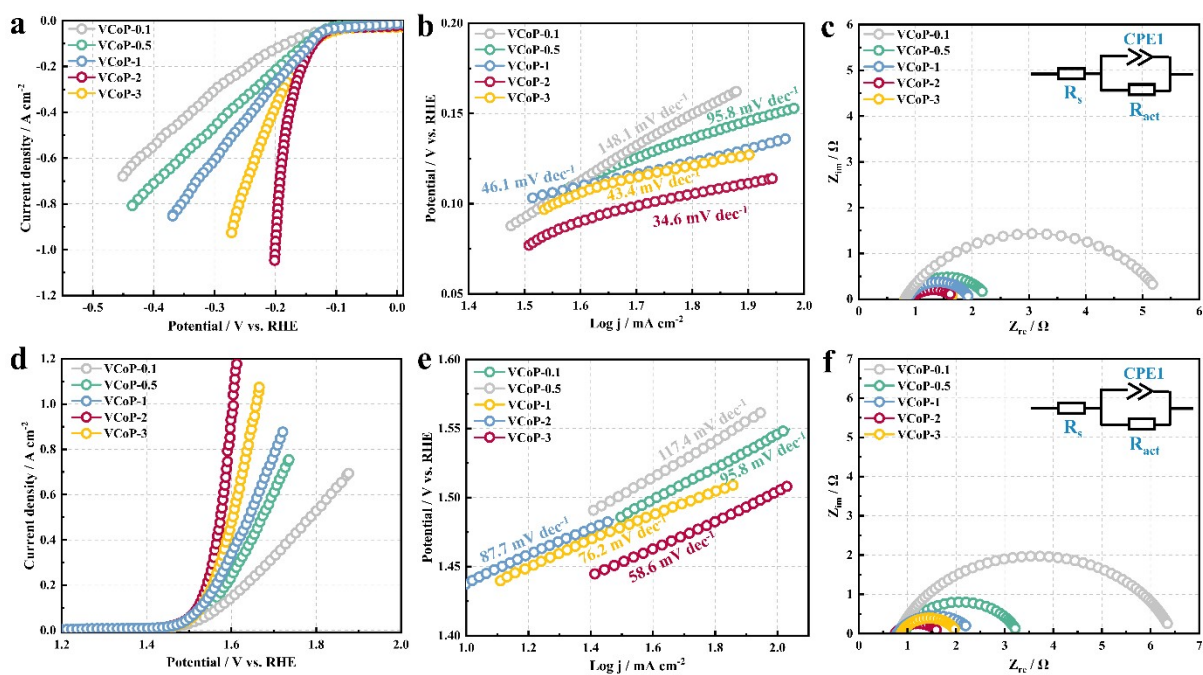


Figure S25. (a) Linear sweep voltammograms (LSVs) of VCoP/porous Ni foam prepared by different elec-trodeposition current densities (100, 500, 1000, 2000 and 3000 mA cm<sup>-2</sup>) for HER. The corre-sponding (b) Tafel plots and (c) EIS plots. (d) LSVs of VCoP/ porous Ni foam prepared by different elec-trodeposition current densities (100, 500, 1000, 2000 and 3000 mA cm<sup>-2</sup>) for OER. The corre-sponding (e) Tafel plots and (f) EIS plots.

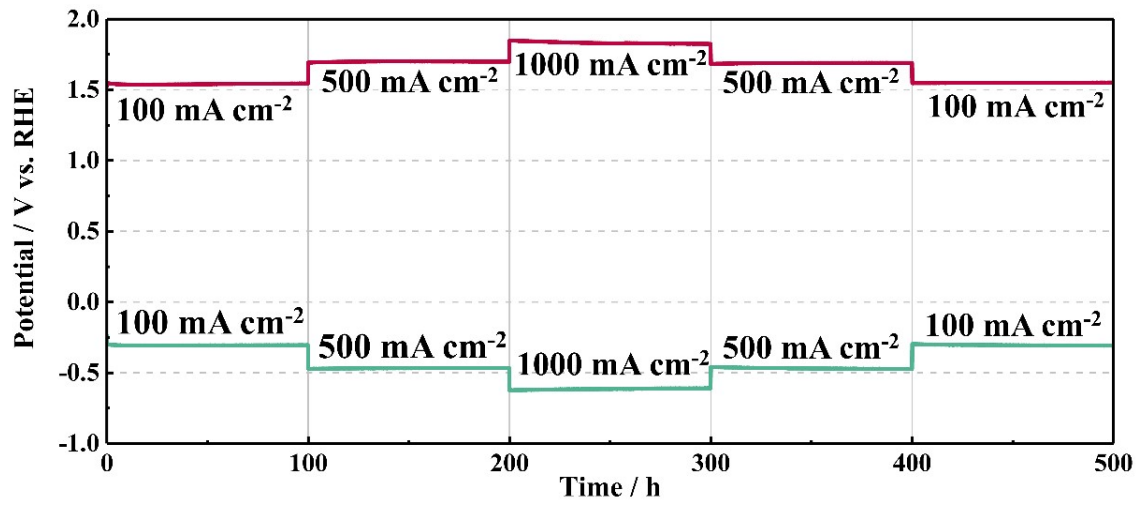


Figure S26. The long-term stability test of the VCoP/porous Ni foam for OER and HER.

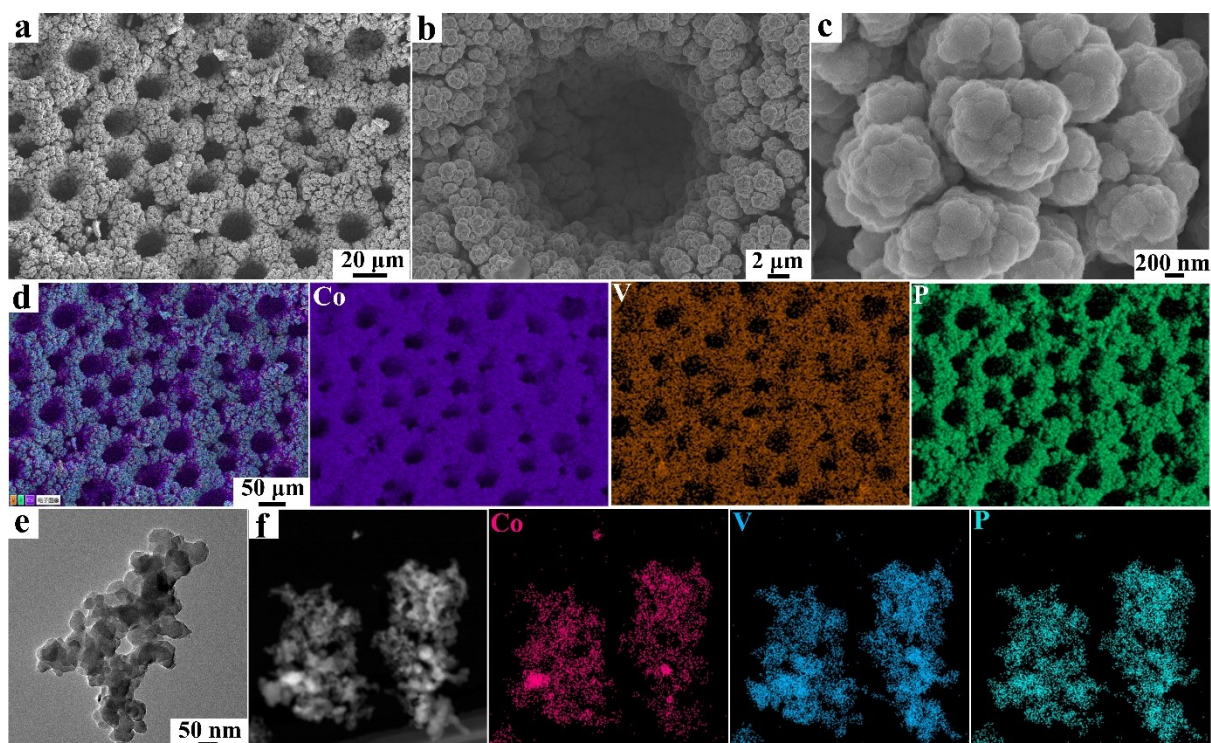


Figure S27. SEM images (a-c) and the corresponding EDS elemental mapping of Co, V and P elements of VCoP-2/NF samples after HER stability tests. (e) TEM image and (f) corresponding EDS element mapping of Co, V and P elements after HER stability tests.

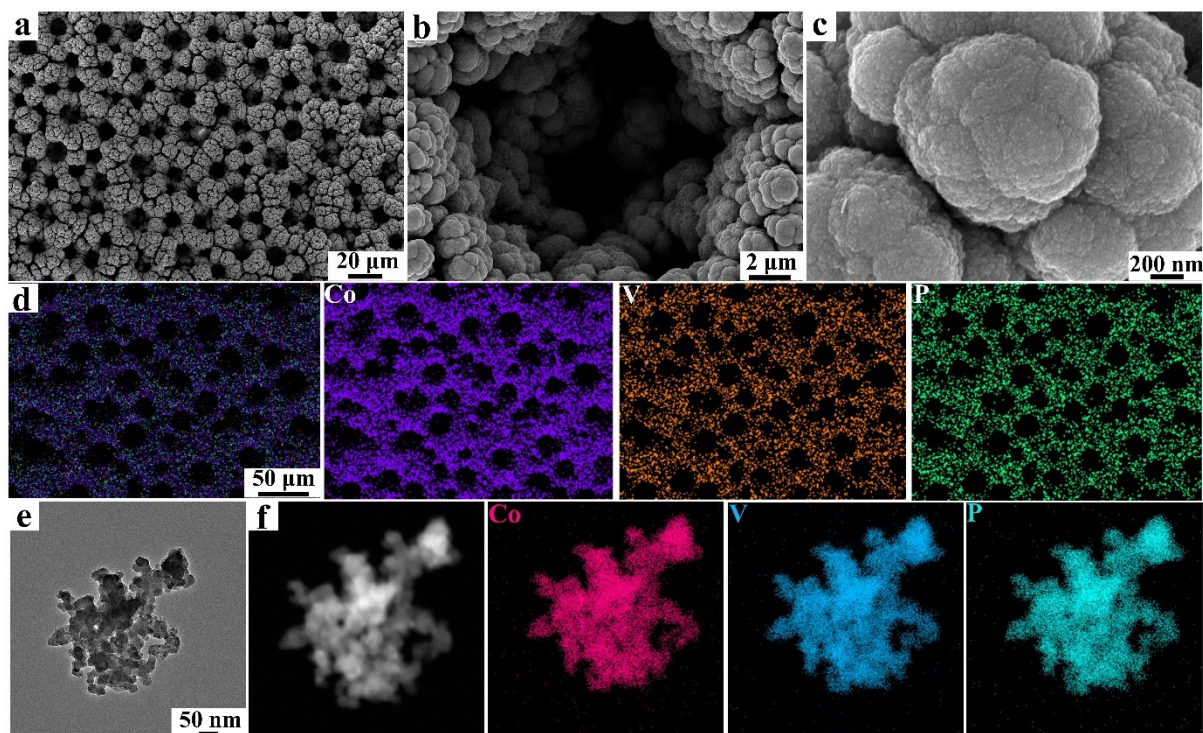


Figure 28. SEM images (a-c) and the corresponding EDS elemental mapping of Co, V and P elements of VCoP-2/NF samples after OER stability tests. (e) TEM image and (f) corresponding EDS element mapping of Co, V and P elements after OER stability tests.

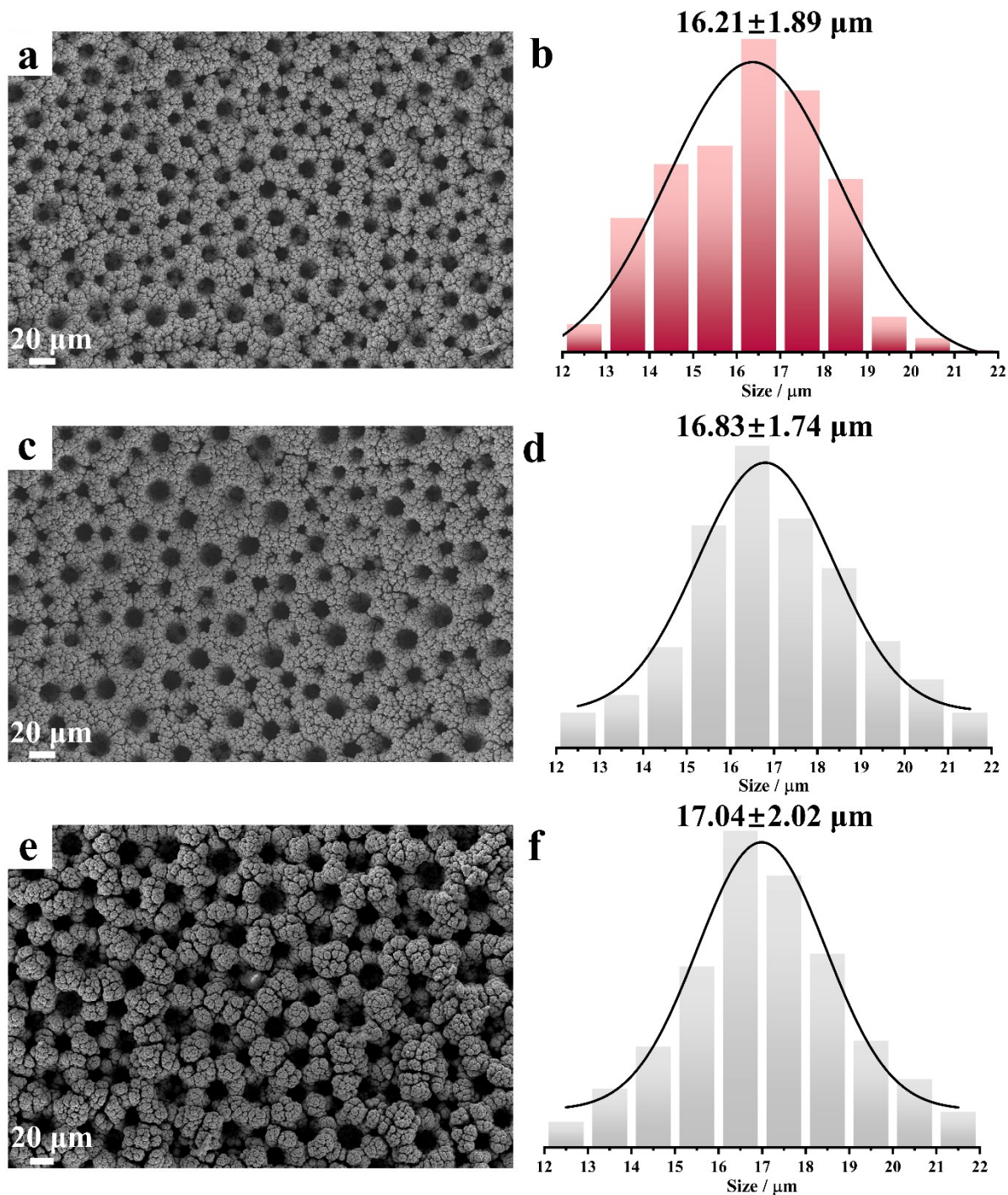


Figure S29. (a) SEM image and (b) the histogram of cavity diameter distribution of porous VCoP-2 foams before the stability tests. (c) SEM image and (d) the histogram of cavity diameter distribution of porous VCoP-2 foams after the HER stability test. (e) SEM image and (f) the histogram of cavity diameter distribution of porous VCoP-2 foams after the OER stability test.

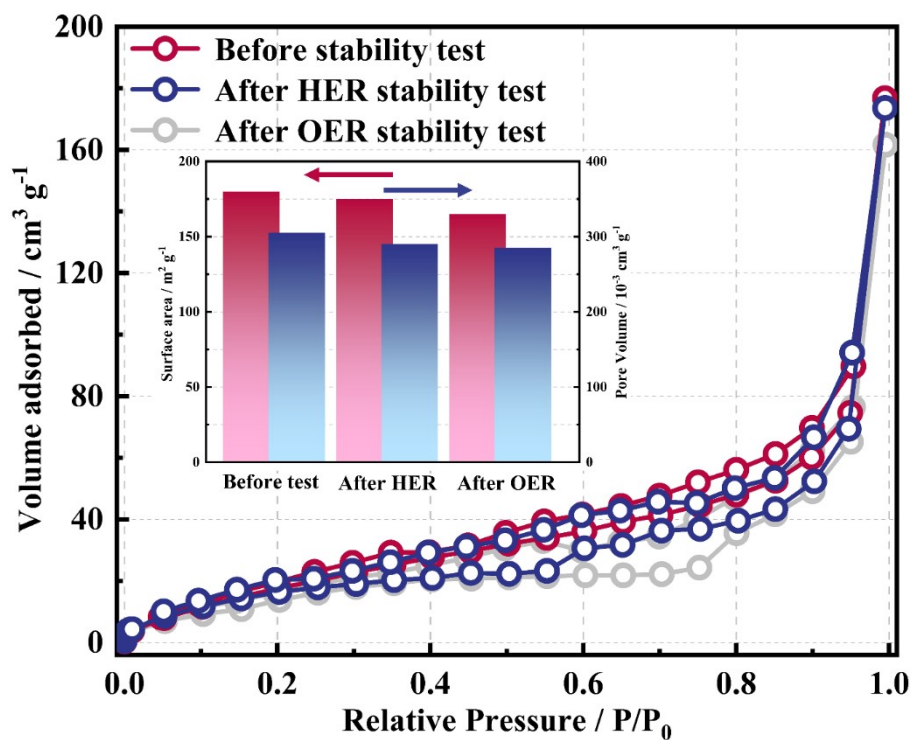


Figure S30. Nitrogen adsorption-desorption isotherms for the samples of VCoP-2 before stability test and after HER and OER stability test, with a comparison of corresponding surface area and pore volume (inset).

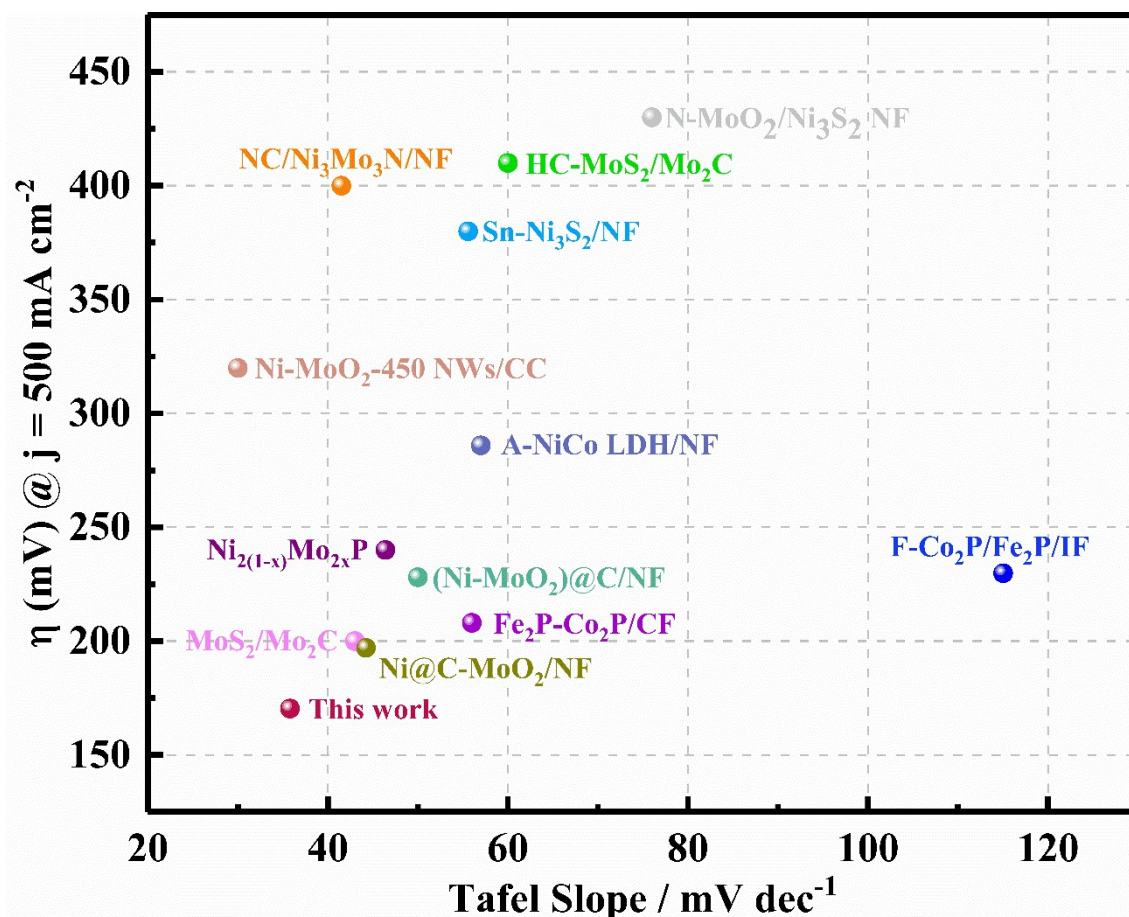


Figure S31. Comparison of HER overpotentials ( $\eta$ ) and Tafel slope of the VCoP-2/NF obtained at 500 mA cm<sup>-2</sup> with reported literatures (A-NiCo LDH/NF<sup>3</sup>, F-Co<sub>2</sub>P/Fe<sub>2</sub>P/IF<sup>4</sup>, Fe<sub>2</sub>P-Co<sub>2</sub>P/CF<sup>5</sup>, (Ni-MoO<sub>2</sub>)@C/NF<sup>6</sup>, Ni-MoO<sub>2</sub>-450 NWs/CC<sup>7</sup>, NC/Ni<sub>3</sub>Mo<sub>3</sub>N/NF<sup>8</sup>, MoS<sub>2</sub>/Mo<sub>2</sub>C<sup>9</sup>, Sn-Ni<sub>3</sub>S<sub>2</sub>/NF<sup>10</sup>, N-MoO<sub>2</sub>/Ni<sub>3</sub>S<sub>2</sub> NF<sup>11</sup> and Ni@C-MoO<sub>2</sub>/NF<sup>12</sup>)



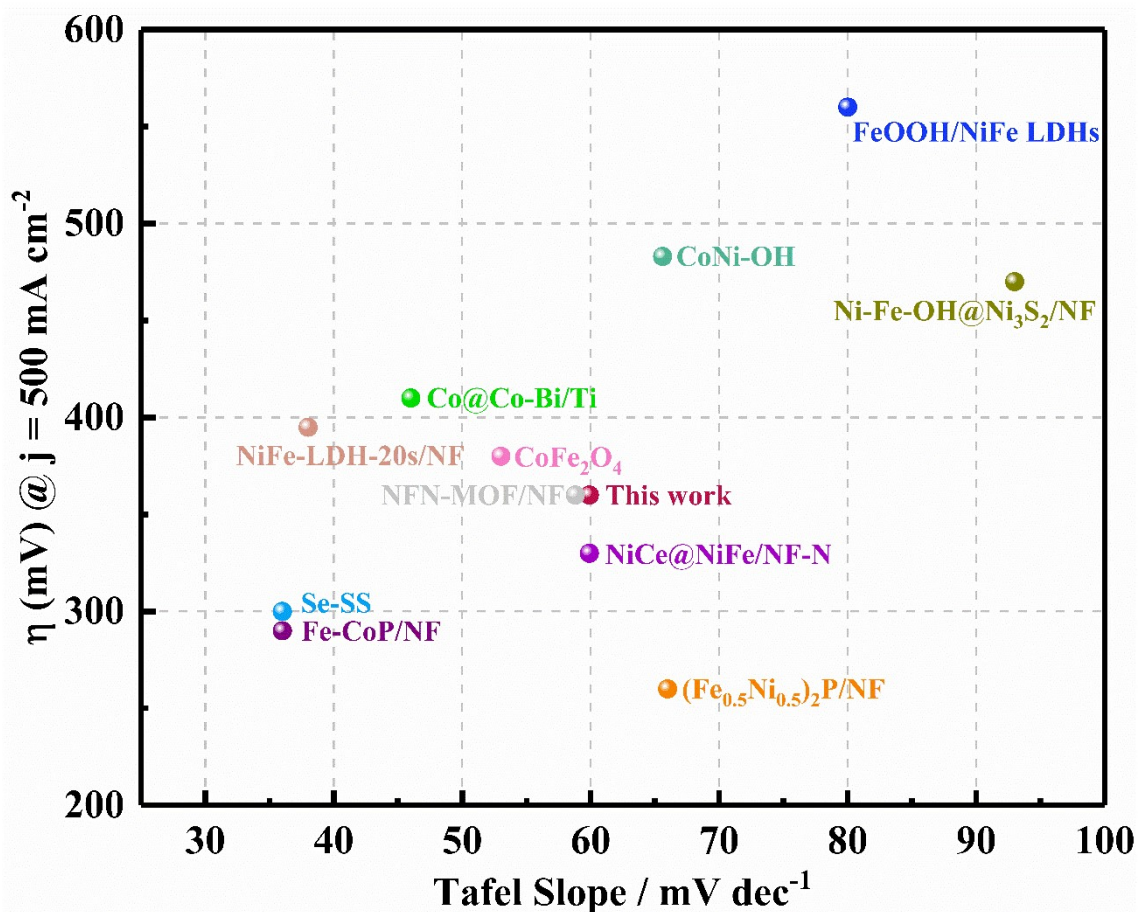


Figure S32. Comparison of OER overpotentials ( $\eta$ ) and Tafel slope of the VCoP-2/NF obtained at  $500 \text{ mA cm}^{-2}$  with reported literatures (NiCe@NiFe/NF-N<sup>13</sup>, (Fe<sub>0.5</sub>Ni<sub>0.5</sub>)<sub>2</sub>P/NF<sup>14</sup>, FeOOH/NiFe LDHs<sup>15</sup>, CoFe<sub>2</sub>O<sub>4</sub><sup>16</sup>, CoNi-OH<sup>17</sup>, Fe-CoP/NF<sup>18</sup>, NFN-MOF/NF<sup>19</sup>, Co@Co-Bi/Ti<sup>20</sup>, Se-SS<sup>21</sup>, NiFe-LDH-20s/NF<sup>22</sup> and N-Fe-OH@Ni<sub>3</sub>S<sub>2</sub>/NF<sup>23</sup>)

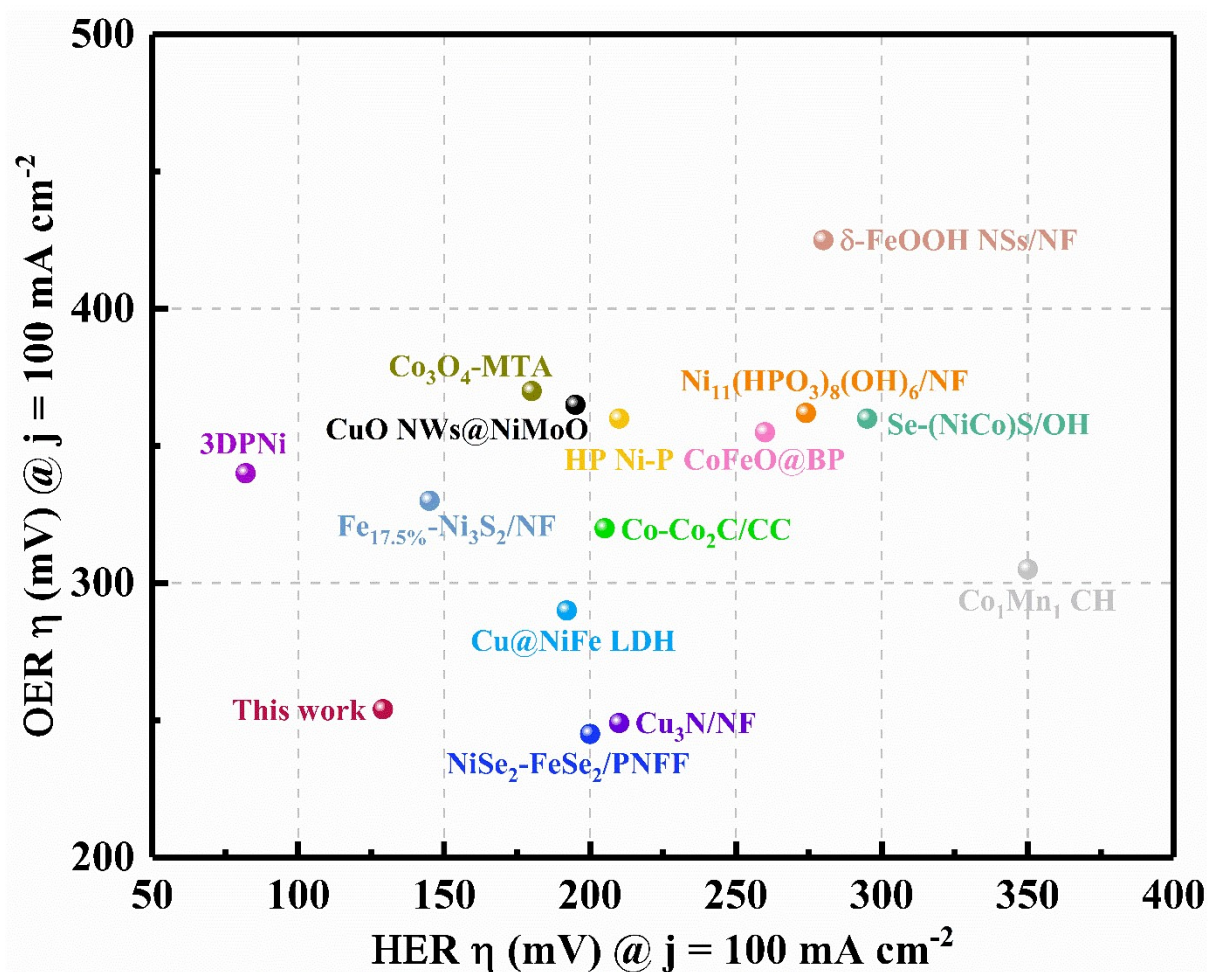


Figure S33. Plots to compare HER and OER overpotentials ( $\eta$ ) of VCoP-2/NF obtained at  $100 \text{ mA cm}^{-2}$  with reported literatures ( $\text{Ni}_{11}(\text{HPO}_3)_8(\text{OH})_6/\text{NF}$ <sup>24</sup>,  $\text{CoFeO@BP}$ <sup>25</sup>,  $\text{Cu@NiFe LDH}$ <sup>26</sup>,  $\text{Co}_1\text{Mn}_1 \text{ CH}$ <sup>27</sup>,  $\text{Fe}_{17.5\%}\text{-Ni}_3\text{S}_2/\text{NF}$ <sup>28</sup>,  $\text{CuO NWs@NiMoO}$ <sup>29</sup>,  $\text{HP Ni-P}$ <sup>30</sup>,  $\text{Cu}_3\text{N}$ <sup>31</sup>,  $\text{Co-Co}_2\text{C/CC}$ <sup>32</sup>,  $\delta\text{-FeOOH NSs/NF}$ <sup>33</sup>,  $\text{NiSe}_2\text{-FeSe}_2/\text{PNFF}$ <sup>34</sup>,  $3\text{DDPNi}$ <sup>35</sup>,  $\text{Co}_3\text{O}_4 \text{ MTA}$ <sup>36</sup> and  $\text{Se}(\text{NiCo})\text{S}_x/(\text{OH})_x$ <sup>37</sup>).

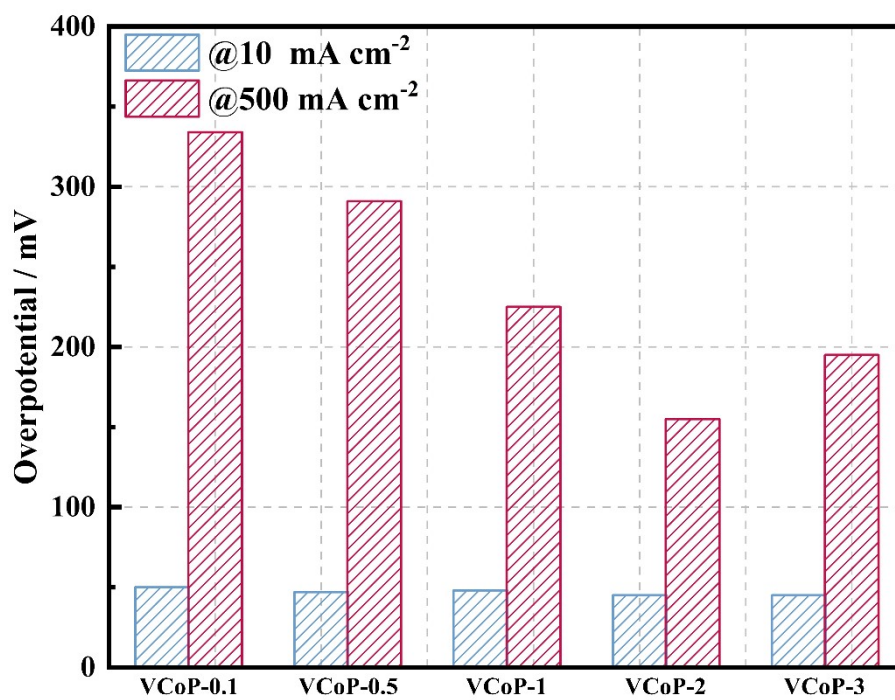


Figure S34. The overpotential required at the current density of 10 and 500 mA cm<sup>-2</sup> for VCoP foams toward HER.

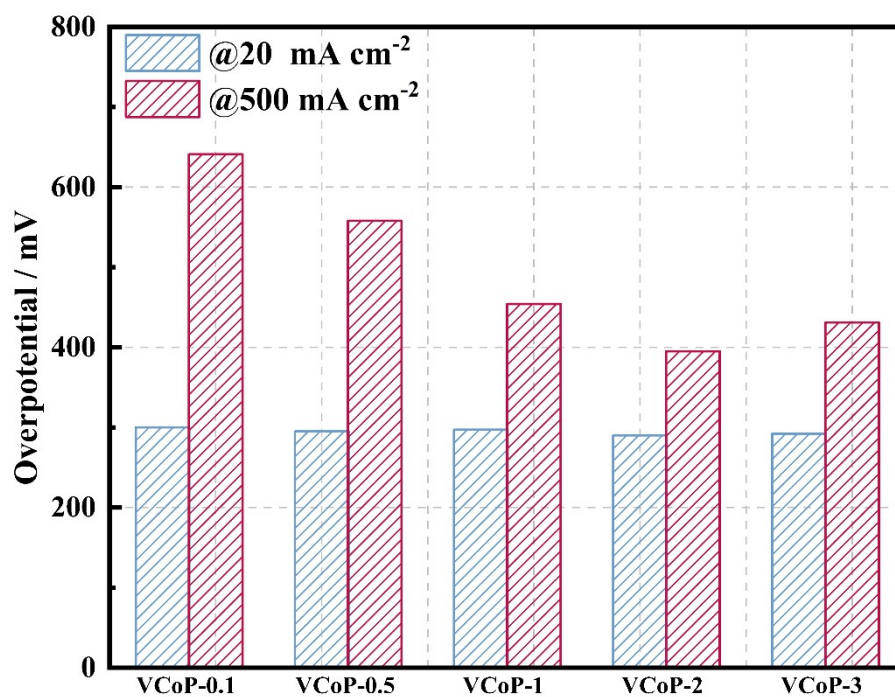


Figure S35. The overpotential required at the current density of 20 and 500 mA cm<sup>-2</sup> for VCoP foams toward OER.

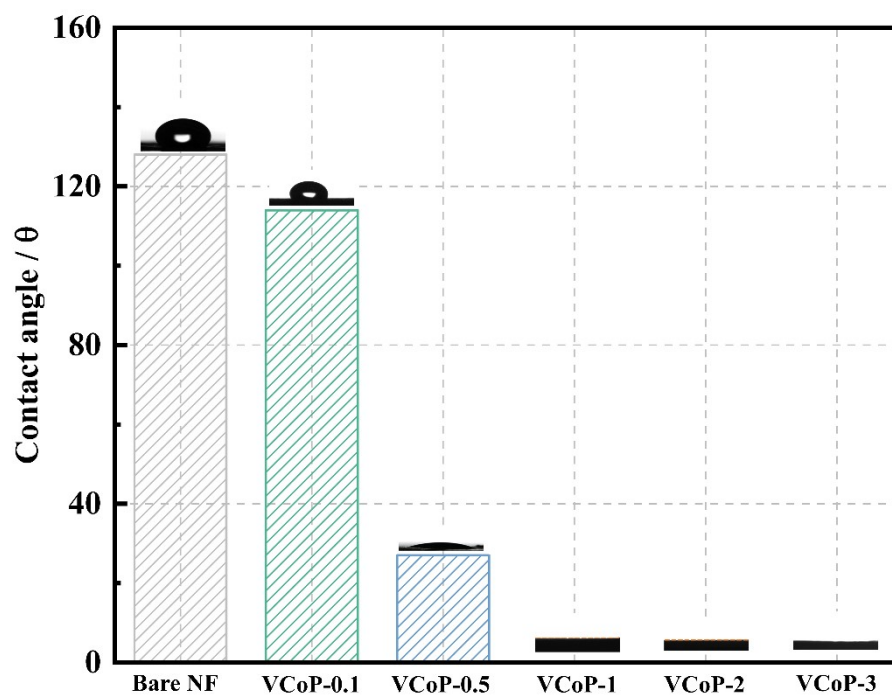


Figure S36. Contact angle of alkaline liquid droplets on the surface of bare NF and porous VCoP foams.

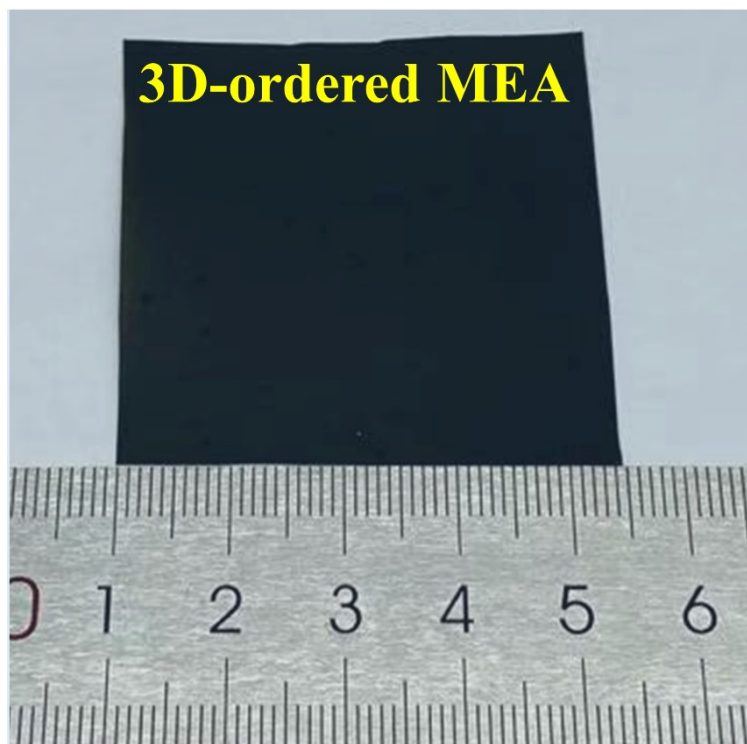


Figure S37. Contact angle of alkaline liquid droplets on the surface of bare NF and porous VCoP foams.

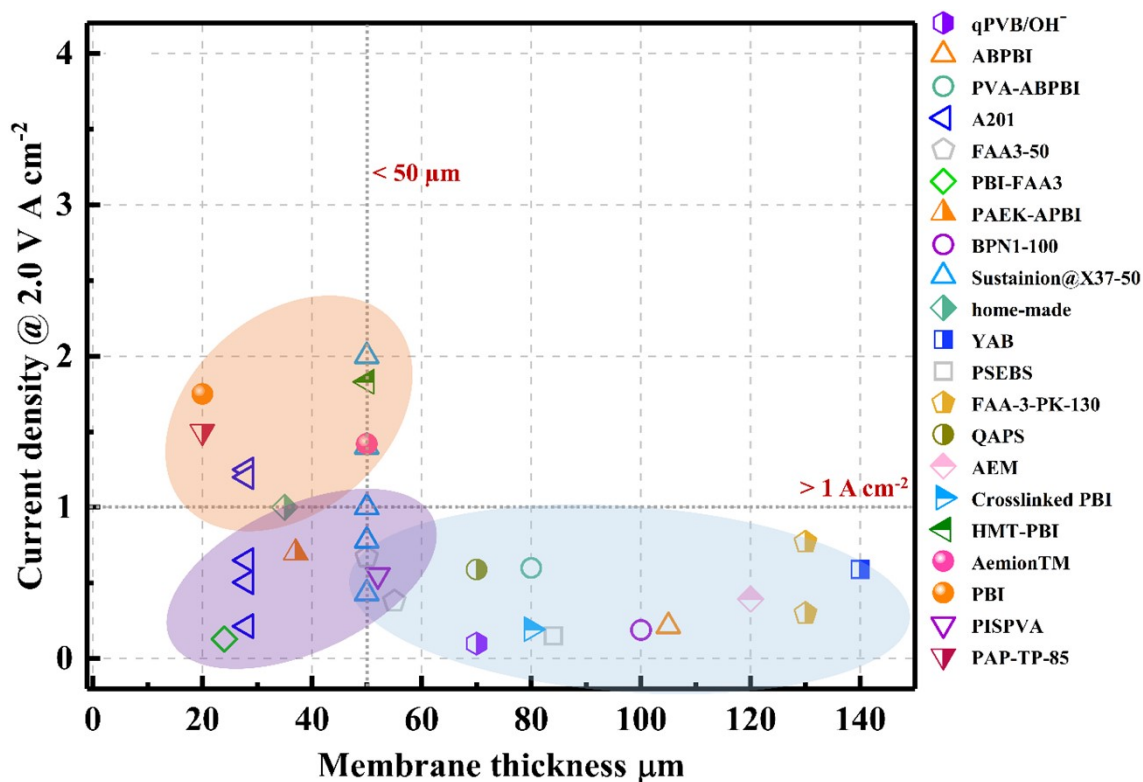


Figure S38. Comparison of alkaline water electrolysis in terms of current density at the voltage of 2.0 V and membrane thickness (qPVB/OH<sup>-</sup><sup>38</sup>; ABPBI<sup>39</sup>; PVA-ABPBI<sup>40</sup>; A201<sup>41-45</sup>; FAA3-50<sup>46, 47</sup>; PBI-FAA3<sup>48</sup>; PAEK-APBI<sup>49</sup>; BPN1-100<sup>50</sup>; Sustainion@X37-50<sup>51-54</sup>; home-made<sup>15</sup>; YAB<sup>55</sup>; PSEBS<sup>56</sup>; FAA-3-PK-130<sup>57,58</sup>; QAPS<sup>59</sup>; AEM<sup>60</sup>; Crosslinked PBI<sup>61</sup>; HMT-PBI<sup>62</sup>; AemionTM<sup>63</sup>; PBI<sup>64</sup>; PISPVA<sup>65</sup>; PAP-TP-85<sup>66</sup>)

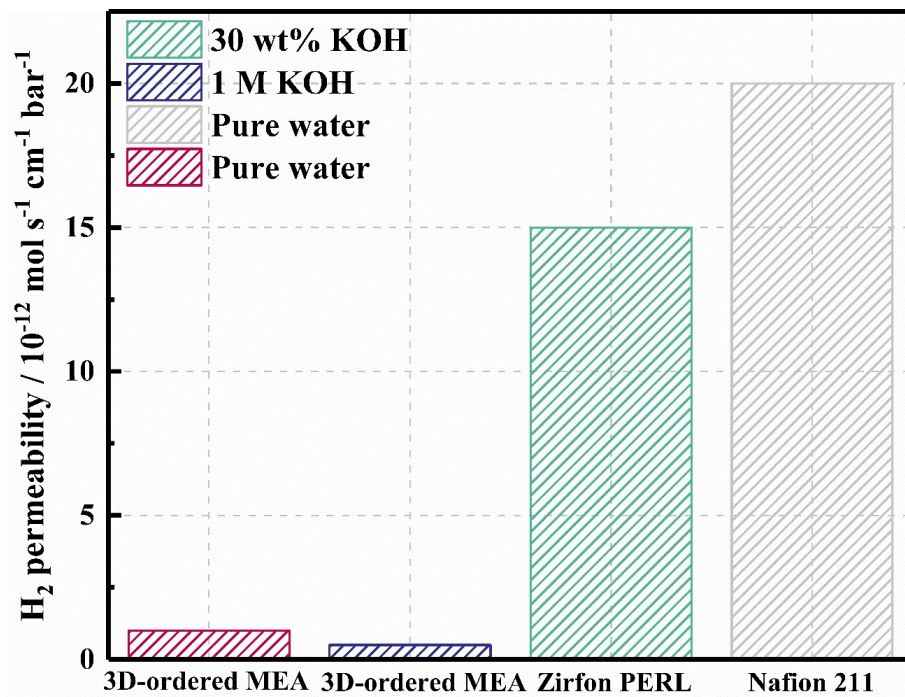


Figure S39. Hydrogen permeability of the novel 3D-ordered MEA-2 and commercial Zirfon<sup>®</sup> PERL and Nafion 211 membrane.



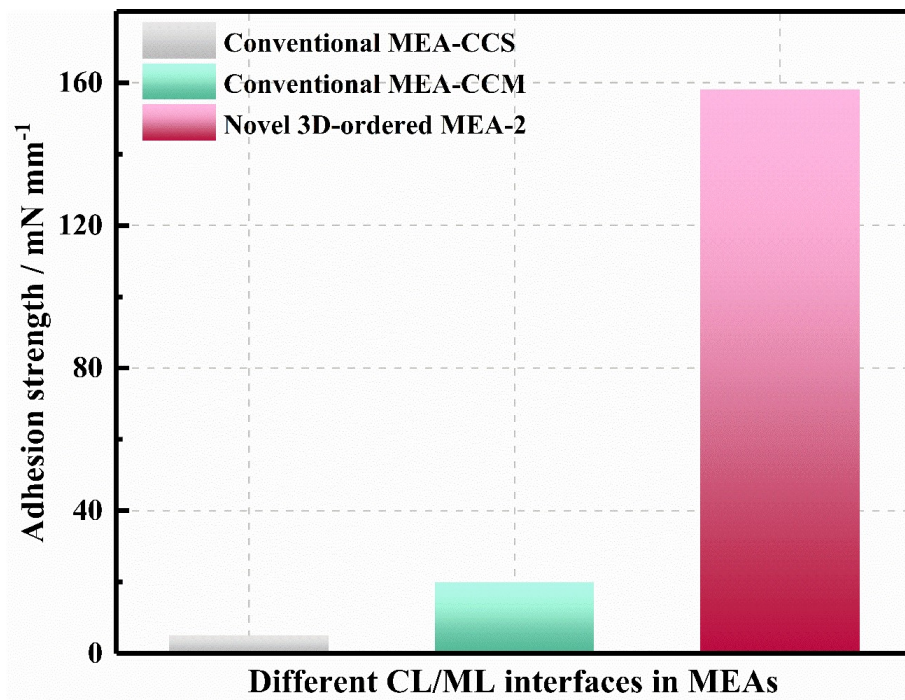


Figure S40. Peeling strengths of the laminates of the CL and ML in conventional MEA-CCS, MEA-CCM and novel 3D-ordered MEA-2.

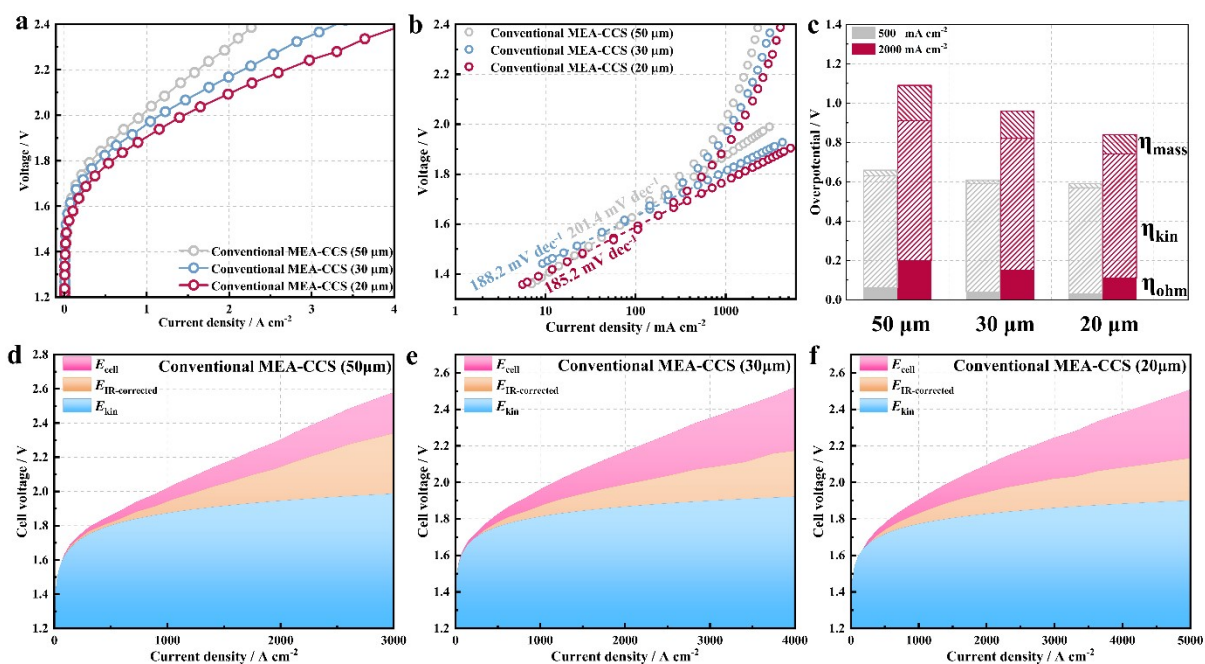


Figure S41. Electrochemical characterization of the alkaline electrolysis with different membrane thickness in 1 M KOH at 60°C. (a) Polarization curves and (b) Tafel plots for conventional MEA-CCS with different membrane thickness: 50, 30 and 20  $\mu\text{m}$ . (c) Overvoltage subdivision of the alkaline electrolysis. The overvoltage of the alkaline electrolysis was subdivided into ohmic overvoltage ( $\eta_{\text{ohm}}$ ), kinetic overvoltage ( $\eta_{\text{kin}}$ ) and mass-transfer overvoltage ( $\eta_{\text{mass}}$ ) at low and high current density region. The cell voltage, iR-corrected voltage and kinetic voltage for the alkaline electrolyzer with (d) conventional MEA-CCS (50  $\mu\text{m}$ ), (e) conventional MEA-CCS (30  $\mu\text{m}$ ) and conventional MEA-CCS (20  $\mu\text{m}$ ).

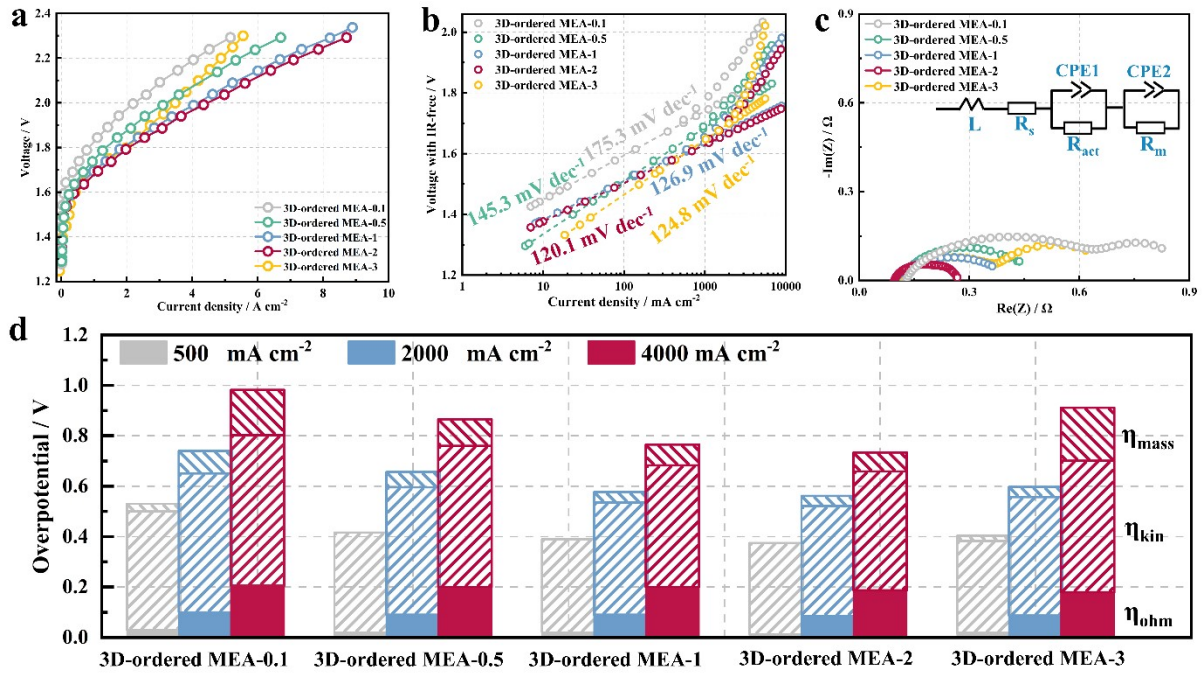


Figure S42. (a) Polarization curves of AEMWE with different 3D-ordered MEAs recorded at 60 °C in 1 M KOH solution. (b) Tafel plot of the iR-free voltage data from Fig. 5a for different 3D-ordered MEAs. (c) EIS measurements were obtained during alkaline electrolyzers operation at 1.8 V<sub>cell</sub>. (d) The overvoltage of alkaline electrolyzers was subdivided into ohmic overvoltage ( $\eta_{ohm}$ ), kinetic overvoltage ( $\eta_{kin}$ ) and mass-transfer overvoltage ( $\eta_{mass}$ ) at low (500 mA cm<sup>-2</sup>) and high (2000 and 4000 mA cm<sup>-2</sup>) current density region.

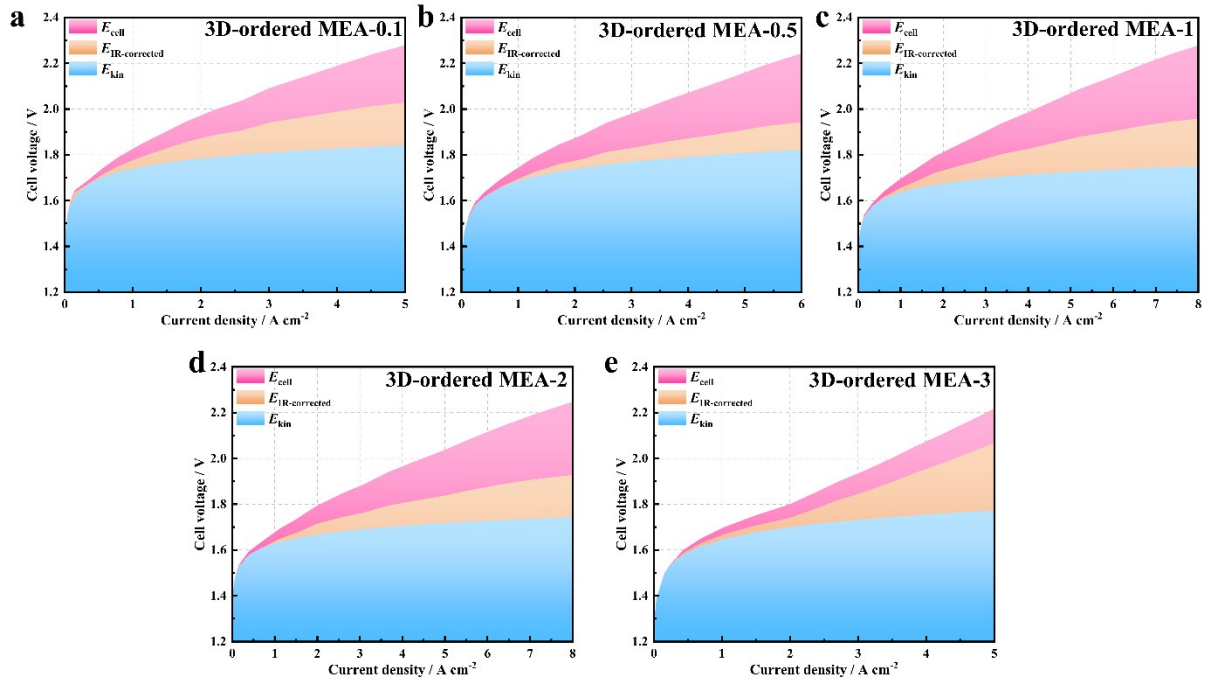


Figure S43. The cell voltage, iR-corrected voltage and kinetic voltage for the alkaline electrolyzer with (a) 3D-ordered MEA-0.1, (b) 3D-ordered MEA-0.5, (c) 3D-ordered MEA-1, (d) 3D-ordered MEA-2, (e) 3D-ordered MEA-2 and (e) 3D-ordered MEA-3.

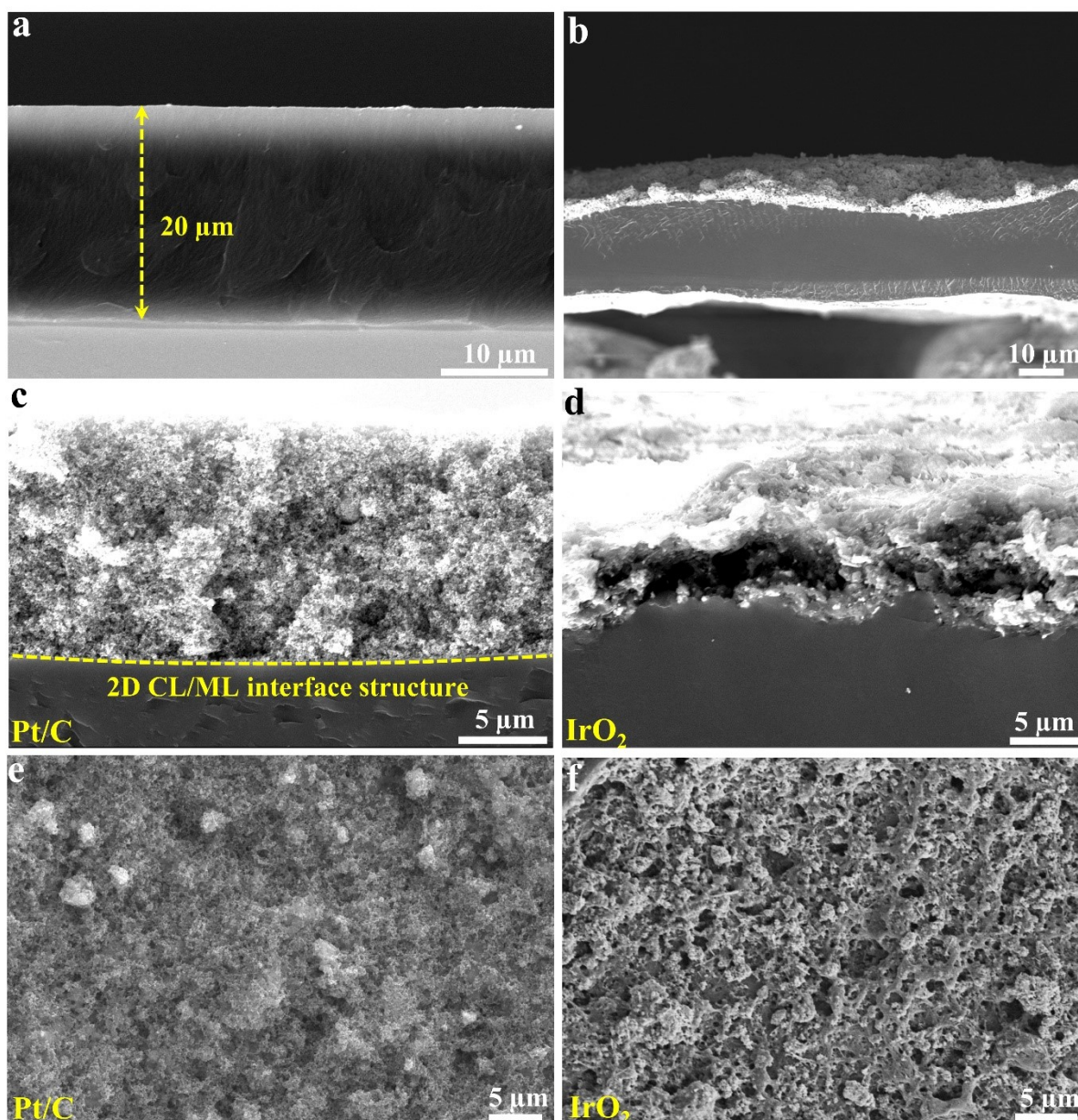


Figure S44. SEM images of the cross-section of (a) bare membrane, (b) the conventional MEA-CCM, (c) cathode catalyst layer (Pt/C) and anode catalyst layer (IrO<sub>2</sub>). SEM images of the surface of (e) cathode catalyst layer and (f) anode catalyst layer.

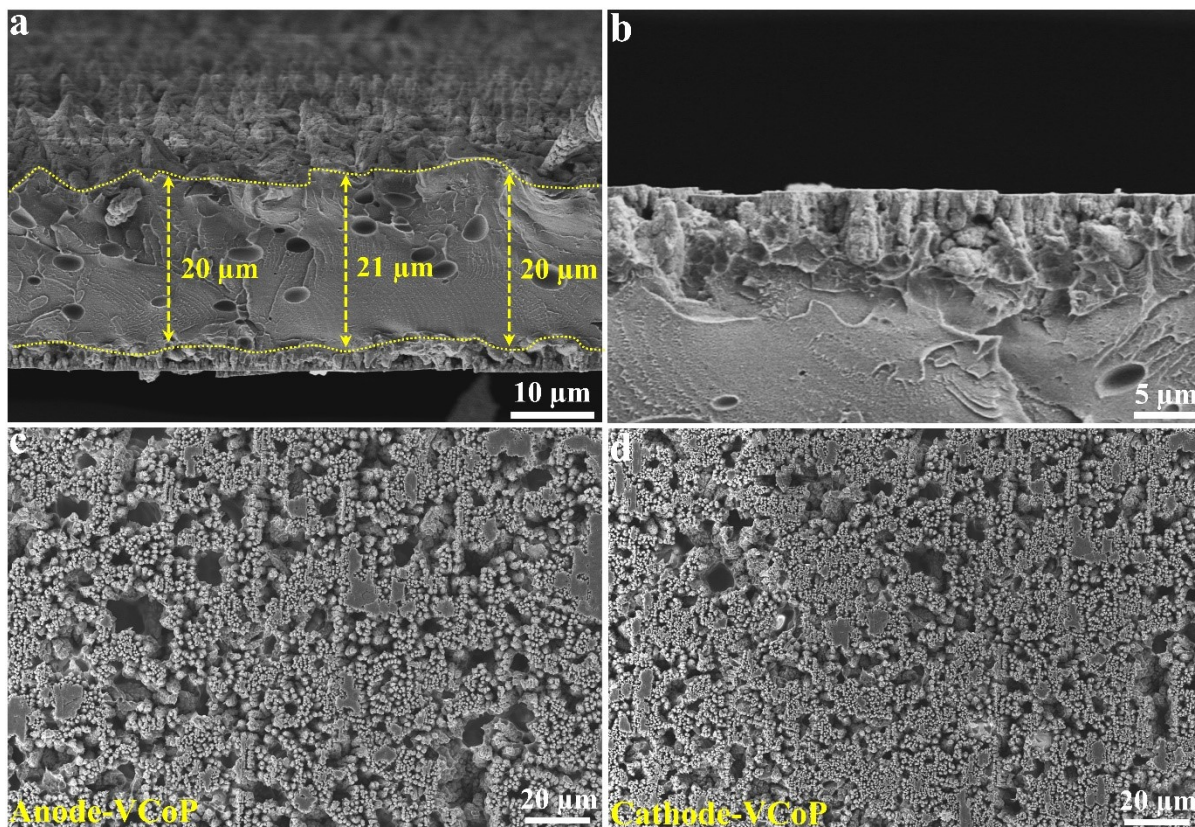


Figure S45. SEM images of the cross-section of (a) the conventional 3D-ordered MEA and (b) catalyst layer (VCoP-2). SEM images of the surface of (c) cathode catalyst layer and (d) anode catalyst layer.

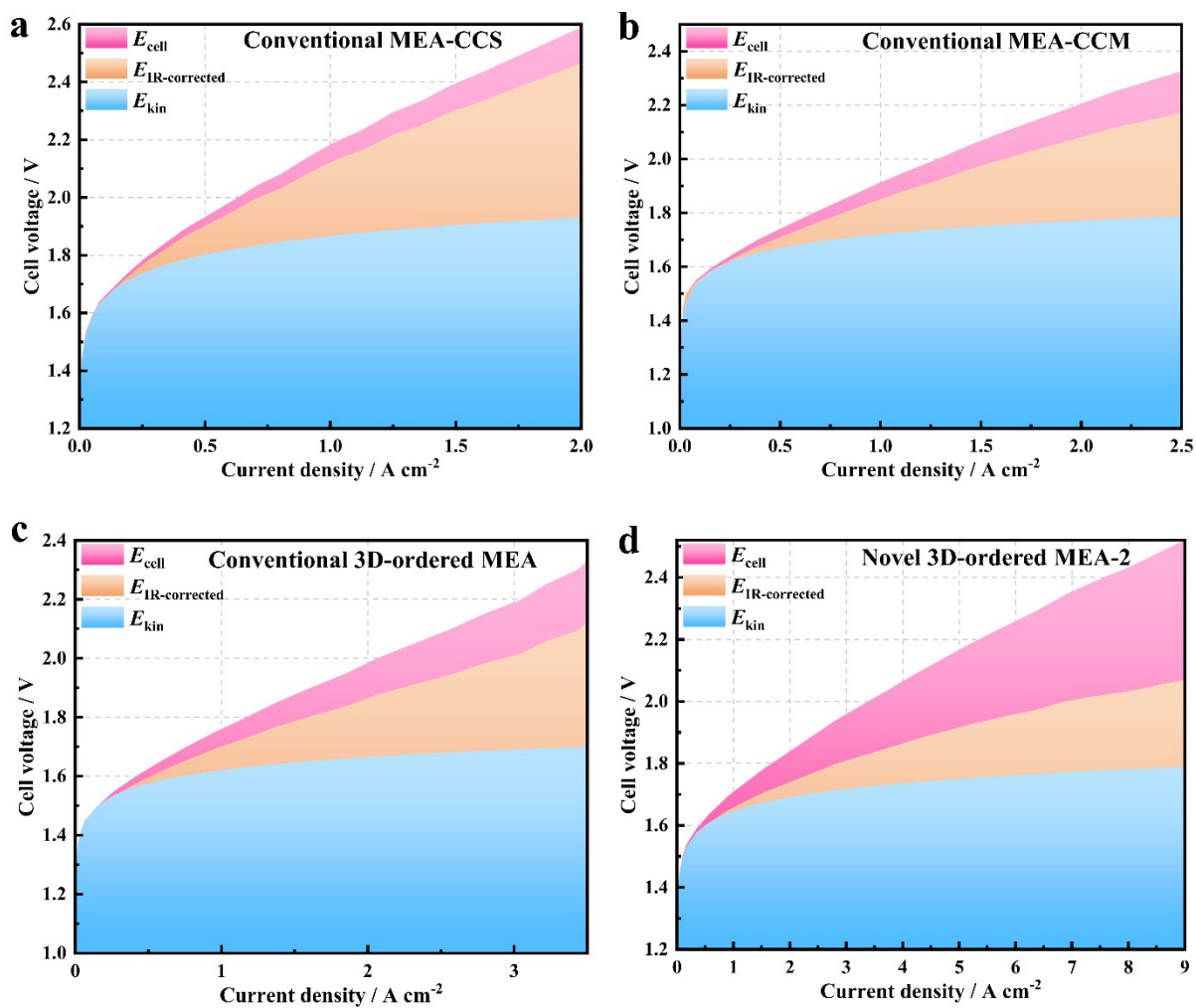


Figure S46. The cell voltage,  $iR$ -corrected voltage and kinetic voltage for the alkaline electrolyzer with (a) conventional MEA-CCS, (b) conventional MEA-CCM, (c) conventional 3D-ordered MEA and (d) novel 3D-ordered MEA-2.

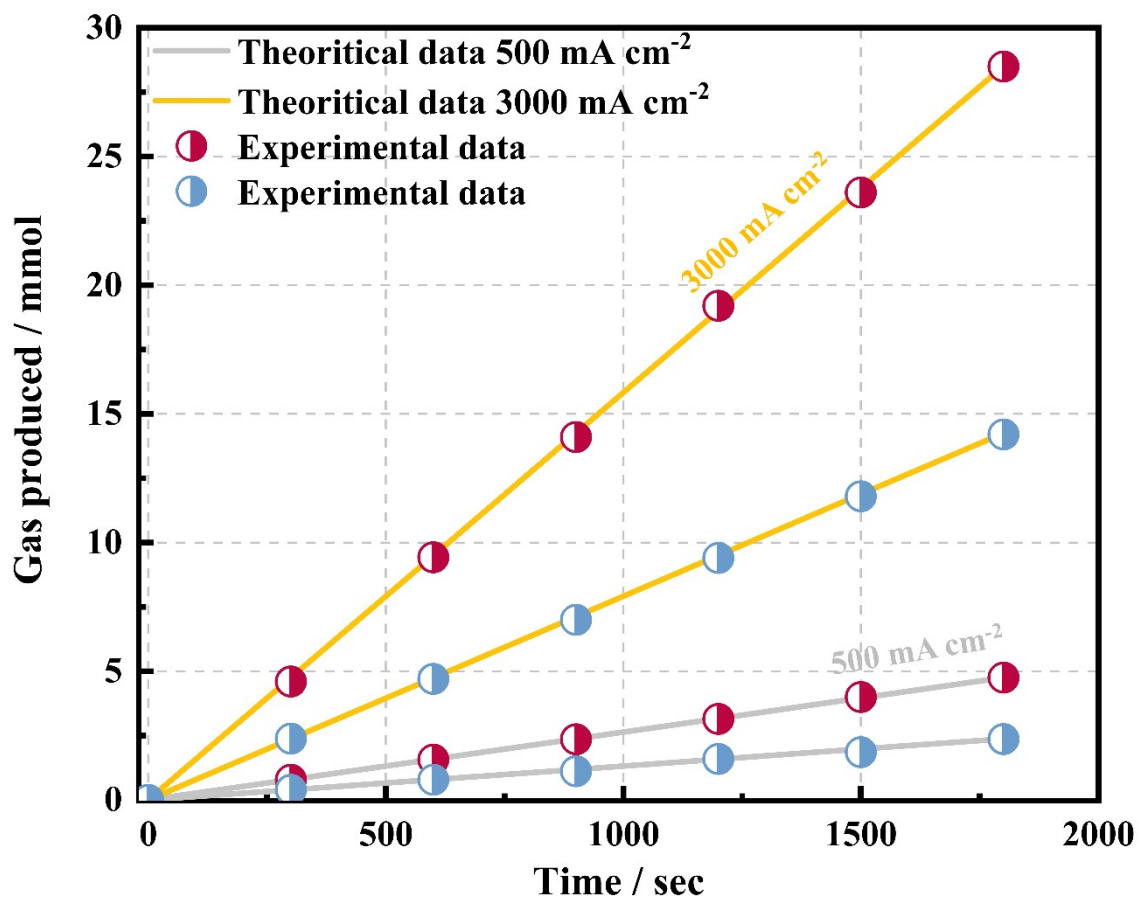


Figure S47. Amount of H<sub>2</sub> and O<sub>2</sub> collected by the water drainage method as a function of time.



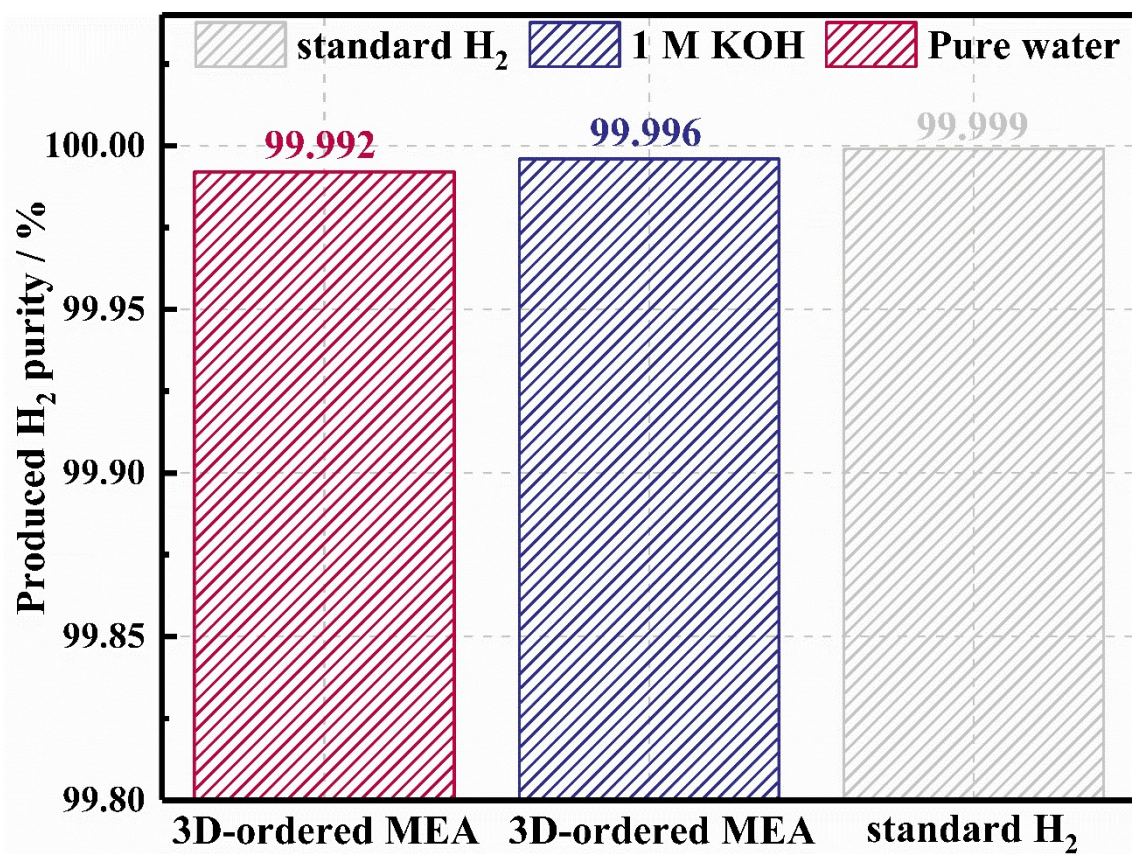


Figure S48. Hydrogen gas purity generated from the novel 3D-ordered MEA-2. Produced H<sub>2</sub> gas was measured by gas-chromatography (GC) and compared with standard H<sub>2</sub> gas (99.999 %).

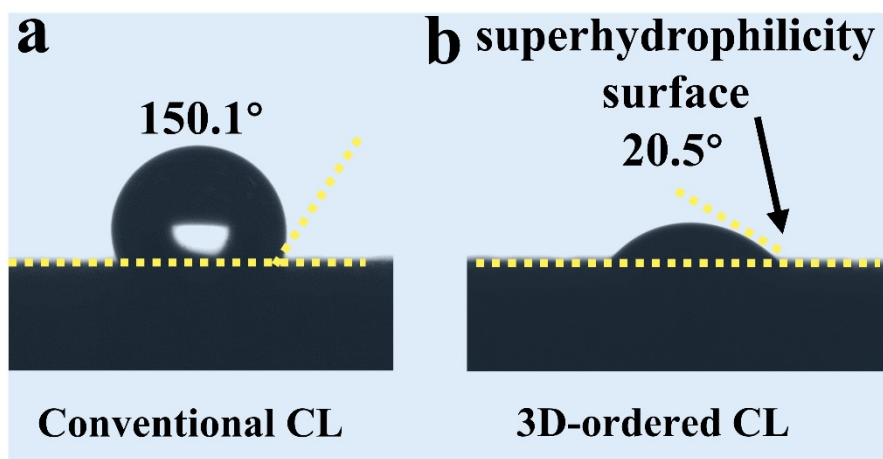


Figure S49. Contact angle of water droplets on the surface of the (a) conventional CL and (b) novel 3D-ordered CL.

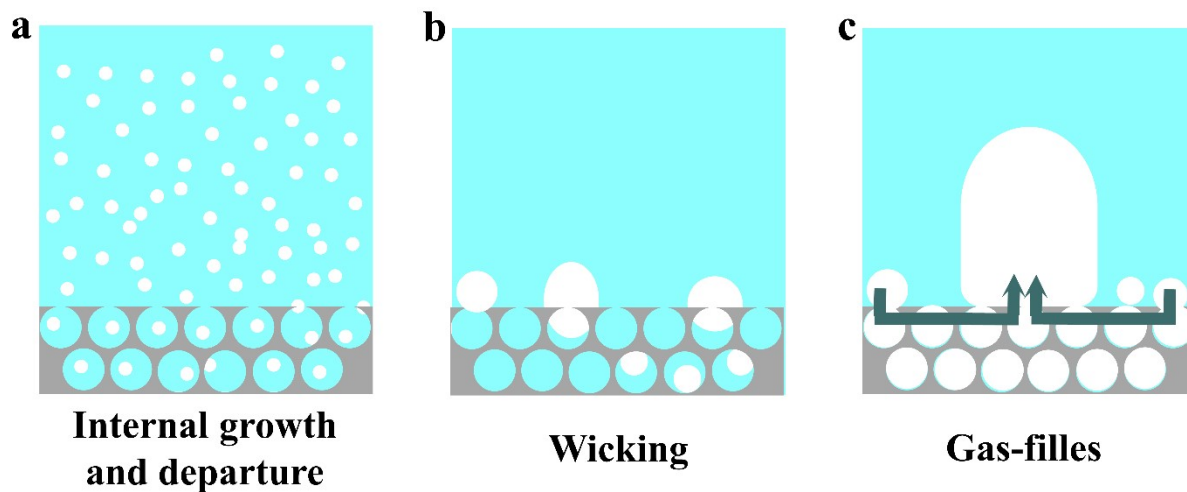


Figure S50. Schematics of bubble growth and departure modes<sup>67</sup>.

- (a) Hydrophilic electrode and the bubble departure size smaller than the pore size.
- (b) Hydrophilic electrode and the bubble departure size comparable to or larger than the pore size.
- (c) Hydrophobic electrode where the bubble departure size dictated by the macroscopic receding contact angle.

Table S1. Physical properties of VCoP-0.1, VCoP-0.5, VCoP-1, VCoP-2 and VCoP-3.

	VCoP-0.1	VCoP-0.5	VCoP-1	VCoP-2	VCoP-3
Electrical resistivity / mΩ cm	0.78	0.82	0.85	0.96	0.95
Porosity / %	0.46	0.96	0.95	0.95	0.95
Pore diameter / μm	1.12 ± 0.28	6.53 ± 1.25	12.35 ± 1.81	16.87 ± 2.09	15.34 ± 2.12 μm
Specific surface area / m <sup>2</sup> m <sup>-3</sup>	3.1 × 10 <sup>3</sup>	8.9 × 10 <sup>3</sup>	2.1 × 10 <sup>4</sup>	3.1 × 10 <sup>4</sup>	2.7 × 10 <sup>4</sup>
Hole depth / μm	0~4	4~8	8~14	15~25	30~60

Table S2. Properties of the *m*-PBI membrane applied in this work.

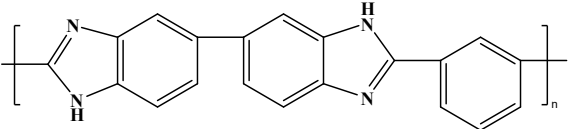
<i>m</i> -PBI	
KOH doping / M	1
Swelling degree (%) @ 60 °C	25
Water uptake (%) @ 60 °C	13
$\sigma$ (mS/cm) @ 60 °C	76

Table S3. Properties of the poly(alkyl-terphenyl piperidinium) membrane applied in this work.

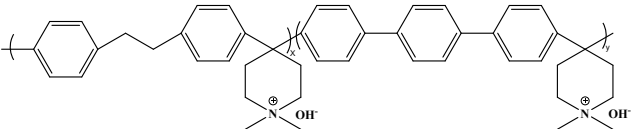
poly(alkyl-terphenyl piperidinium)	
IEC (mmol/g)	2.70
Swelling degree (%) @ 60 °C	97
Water uptake (%) @ 60 °C	600
$\sigma$ (mS/cm) @ 60 °C	123

Table S4. The comparisons of the energy efficiency of the 3D-ordered MEAs with state-of-the-art examples in 1 M KOH.

Anode	Cathode	Membrane	Current density / mA cm <sup>-2</sup>	Temperatur e / °C	Energy efficiency / %	Ref.
Li <sub>x</sub> Co <sub>3-x</sub> O <sub>4</sub>	Ni	QPDTB	300	45	69.88%	68
Cu <sub>0.7</sub> Co <sub>2.3</sub> O <sub>4</sub>	Ni	QPVB	300	55	61.30%	38
Ni foam	Ni foam	ABPBI	200	50	72.66%	39
Ni foam	Ni foam	PVA-ABPBI	500	70	73.29%	40
IrO <sub>2</sub>	Pt/C	A201	1000	50	74.93%	41
NiMnO <sub>x</sub>	Pt/C	FAA-3-50	500	50	77.77%	46
Ni foam	Ni foam	PF-41	1000	60	56.31%	48
Ni foam	Ni foam	PAEK-APBI	2000	60	60.10%	49
IrO <sub>2</sub>	Pt/C	BPN1-100	500	50	63.94%	50
Cu <sub>0.81</sub> Co <sub>2.19</sub> O <sub>4</sub>	Co <sub>3</sub> S <sub>4</sub>	Sustainion® X37-50	1000	50	65.40%	51
FeOOH/NiFe LDHs	Pt/C	Home-made	1000	70	71.09%	15
Ni <sub>12</sub> P <sub>5</sub> /Ni <sub>3</sub> (PO <sub>4</sub> ) <sub>2</sub> - HS	Ni <sub>12</sub> P <sub>5</sub> /Ni <sub>3</sub> (PO <sub>4</sub> ) <sub>2</sub> - HS	YAB	1000	50	62.01%	55
Ni <sub>0.75</sub> Fe <sub>2.25</sub> O <sub>4</sub>	Pt/C	Sustainion® X37-50 Grade T	1000	45	82.69%	52
Ni foam	Ni foam	PSEBS-CM- DABCO	100	45	75.15%	56

Ni	Ni	A201	200	70	78.12%	69
CuCoO <sub>x</sub>	Ni/(CeO <sub>2</sub> -La <sub>2</sub> O <sub>3</sub> )	A201	1000	80	69.45%	42
NiCoO <sub>x</sub> :Fe	Pt/C	FAA-3	1000	50	57.55%	19
NiFe <sub>2</sub> O <sub>4</sub>	NiFeCo alloy	Sustainion 37–50	500	50	71.94%	70
NiCo <sub>2</sub> O <sub>4</sub>	Pt/C	FAA-3-50	300	50	79.93%	47
CuCoO <sub>x</sub>	Pt/C	A201	1000	50	74.93%	43
NiFe-BTC-GNPs	NiMO <sub>4</sub> /MoO <sub>2</sub>	FAA-3-PK-130	1000	70	78.99%	57
Ni	Ni	Thermally cured PBI	500	80	63.67%	61
CuCo <sub>2</sub> O <sub>4</sub>	Pt/C	Sustainion® X37-50 Grade T	1000	45	78.85%	53
NiAlMo	NiAlMo	HMT-PMBI	2000	60	68.11%	62
Fe-NiMo-NH <sub>3</sub> /H <sub>2</sub>	NiMo-NH <sub>3</sub> /H <sub>2</sub>	Sustainion® X37-50 Grade T	1000	80	75.00%	54
Ir black	Pt/C	Aemion™	2000	50	71.22%	63
NiMo	Ni	m-PBI	2000	80	76.40%	64
IrO <sub>2</sub>	Pt/C	PISPVA	500	60	73.34%	65
IrO <sub>2</sub>	Pt/C	SEBS-Pi	500	50	68.51%	66
NiCo <sub>2</sub> O <sub>4</sub>	Pt/C	Home-made	1000	80	72.48%	71
IrO <sub>2</sub>	Pt/C	QPC-TMA	1000	70	86.17%	72
IrO <sub>2</sub>	Pt/C	QMter-co-Mpi	400	80	67.30%	73
NiCo <sub>2</sub> O <sub>4</sub>	NiCo <sub>2</sub> O <sub>4</sub>	Pani-1.03	400	50	71.94%	74
<b>VCoP</b>	<b>VCoP</b>	<b>PBI</b>	<b>1000</b>	<b>60</b>	<b>84.10%</b>	<b>This work</b>



---

VCoP	VCoP	PBI	2000	60	79.46%	This work
VCoP	VCoP	PBI	4000	60	73.35%	This work

---

Table S5. Comparison of the durability of pure-water-fed AEMWE reported in literatures

Anode	Cathode	AEM	Current density / mA cm <sup>-2</sup>	Durability time / h	Voltage degradation / mV h <sup>-1</sup>	Ref.
Li <sub>0.21</sub> Co <sub>2.79</sub> O <sub>4</sub>	Ni	—	300	11	13.6	68
Pb <sub>2</sub> Ru <sub>2</sub> O <sub>7</sub>	Pt black	PSF-TMA <sup>+</sup>	200	6	145	75
NiFe	NiMo	xQAPS	400	8	5	59
NiFe	PtRu/C	HTMA-DAPP	200	170	1.17	76
IrO <sub>2</sub>	Pt/C	PFOTPh-TMA	200	150	0	77
IrO <sub>2</sub>	Pt black	A201	200	550	0.73	45
Fe <sub>x</sub> Ni <sub>y</sub> OOH-20F	Pt/C	PAP-TP-85	200	170	0.56	78
Fe <sub>x</sub> Ni <sub>y</sub> OOH-20F	Pt/C	PAP-TP-85	500	70	1.81	78
Acta 3030	Acta 4030	Reinforced Sustainion x37-50	500	170	0.81	79
IrO <sub>2</sub>	PtRu/C	HTMA-DAPP	200	24	5	80
IrO <sub>2</sub>	Pt black	PiperION	500	180	0.67	80
VCoP	VCoP	poly(alkyl-terphenyl piperidinium)	500	600	0.05	This work
VCoP	VCoP	poly(alkyl-terphenyl piperidinium)	1000	600	0.1	This work

## References

1. L. Wan, Z. Xu, P. Wang, Y. Lin and B. Wang, *Journal of Membrane Science*, 2021, **618**, 118642.
2. N. Chen, C. Hu, H. H. Wang, S. P. Kim, H. M. Kim, W. H. Lee, J. Y. Bae, J. H. Park and Y. M. Lee, *Angew Chem Int Ed Engl*, 2021, **60**, 7710-7718.
3. H. Yang, Z. Chen, P. Guo, B. Fei and R. Wu, *Applied Catalysis B: Environmental*, 2020, **261**, 118240.
4. X.-Y. Zhang, Y.-R. Zhu, Y. Chen, S.-Y. Dou, X.-Y. Chen, B. Dong, B.-Y. Guo, D.-P. Liu, C.-G. Liu and Y.-M. Chai, *Chemical Engineering Journal*, 2020, **399**, 125831.
5. X. Liu, Y. Yao, H. Zhang, L. Pan, C. Shi, X. Zhang, Z.-F. Huang and J.-J. Zou, *ACS Sustainable Chemistry & Engineering*, 2020, **8**, 17828-17838.
6. G. Qian, J. Chen, L. Luo, T. Yu, Y. Wang, W. Jiang, Q. Xu, S. Feng and S. Yin, *ACS Sustainable Chemistry & Engineering*, 2020, **8**, 12063-12071.
7. B. Ren, D. Li, Q. Jin, H. Cui and C. Wang, *Journal of Materials Chemistry A*, 2017, **5**, 24453-24461.
8. Y. Chen, J. Yu, J. Jia, F. Liu, Y. Zhang, G. Xiong, R. Zhang, R. Yang, D. Sun, H. Liu and W. Zhou, *Applied Catalysis B: Environmental*, 2020, **272**, 118956.
9. Y. Luo, L. Tang, U. Khan, Q. Yu, H. M. Cheng, X. Zou and B. Liu, *Nat Commun*, 2019, **10**, 269.
10. J. Jian, L. Yuan, H. Qi, X. Sun, L. Zhang, H. Li, H. Yuan and S. Feng, *ACS Appl Mater Interfaces*, 2018, **10**, 40568-40576.
11. L. Wang, J. Cao, C. Lei, Q. Dai, B. Yang, Z. Li, X. Zhang, C. Yuan, L. Lei and Y. Hou, *ACS Appl Mater Interfaces*, 2019, **11**, 27743-27750.
12. G. Qian, G. Yu, J. Lu, L. Luo, T. Wang, C. Zhang, R. Ku, S. Yin, W. Chen and S. Mu, *Journal of Materials Chemistry A*, 2020, **8**, 14545-14554.
13. G. Liu, M. Wang, Y. Wu, N. Li, F. Zhao, Q. Zhao and J. Li, *Applied Catalysis B: Environmental*, 2020, **260**, 118199.
14. B. Zhang, Y. H. Lui, H. Ni and S. Hu, *Nano Energy*, 2017, **38**, 553-560.
15. J. Chi, H. Yu, G. Jiang, J. Jia, B. Qin, B. Yi and Z. Shao, *Journal of Materials Chemistry A*, 2018, **6**, 3397-3401.
16. S. Lei, Q.-H. Li, Y. Kang, Z.-G. Gu and J. Zhang, *Applied Catalysis B: Environmental*, 2019, **245**, 1-9.
17. C. Huang, Y. Zhong, J. Chen, J. Li, W. Zhang, J. Zhou, Y. Zhang, L. Yu and Y. Yu, *Chemical Engineering Journal*, 2021, **403**, 126304.
18. L. M. Cao, Y. W. Hu, S. F. Tang, A. Iljin, J. W. Wang, Z. M. Zhang and T. B. Lu, *Adv Sci (Weinh)*, 2018, **5**, 1800949.
19. D. Senthil Raja, X.-F. Chuah and S.-Y. Lu, *Advanced Energy Materials*, 2018, **8**, 1801065.
20. C. Xie, Y. Wang, D. Yan, L. Tao and S. Wang, *Nanoscale*, 2017, **9**, 16059-16065.
21. Y. Xiao, T. Hu, X. Zhao, F. X. Hu, H. B. Yang and C. M. Li, *Nano Energy*, 2020, **75**, 104949.
22. X. Tian, Y. Liu, D. Xiao and J. Sun, *Journal of Power Sources*, 2017, **365**, 320-326.
23. X. Zou, Y. Liu, G.-D. Li, Y. Wu, D.-P. Liu, W. Li, H.-W. Li, D. Wang, Y. Zhang and X. Zou, *Advanced Materials*, 2017, **29**, 1700404.
24. P. W. Menezes, C. Panda, S. Loos, F. Bunschei-Bruns, C. Walter, M. Schwarze, X. Deng, H. Dau and M. Driess, *Energy & Environmental Science*, 2018, **11**, 1287-1298.
25. X. Li, L. Xiao, L. Zhou, Q. Xu, J. Weng, J. Xu and B. Liu, *Angew Chem Int Ed Engl*, 2020, **59**, 21106-21113.
26. L. Yu, H. Zhou, J. Sun, F. Qin, F. Yu, J. Bao, Y. Yu, S. Chen and Z. Ren, *Energy & Environmental Science*, 2017, **10**, 1820-1827.

27. T. Tang, W. J. Jiang, S. Niu, N. Liu, H. Luo, Y. Y. Chen, S. F. Jin, F. Gao, L. J. Wan and J. S. Hu, *J Am Chem Soc*, 2017, **139**, 8320-8328.
28. G. Zhang, Y.-S. Feng, W.-T. Lu, D. He, C.-Y. Wang, Y.-K. Li, X.-Y. Wang and F.-F. Cao, *ACS Catalysis*, 2018, **8**, 5431-5441.
29. S. Sirisomboonchai, X. Li, N. Kitiphatpiboon, R. Channoo, S. Li, Y. Ma, S. Kongparakul, C. Samart, A. Abudula and G. Guan, *Journal of Materials Chemistry A*, 2020, **8**, 16463-16476.
30. D. Song, D. Hong, Y. Kwon, H. Kim, J. Shin, H. M. Lee and E. Cho, *Journal of Materials Chemistry A*, 2020, **8**, 12069-12079.
31. C. Panda, P. W. Menezes, M. Zheng, S. Orthmann and M. Driess, *ACS Energy Letters*, 2019, **4**, 747-754.
32. P. Wang, J. Zhu, Z. Pu, R. Qin, C. Zhang, D. Chen, Q. Liu, D. Wu, W. Li, S. Liu, J. Xiao and S. Mu, *Applied Catalysis B: Environmental*, 2021, **296**, 120334.
33. B. Liu, Y. Wang, H. Q. Peng, R. Yang, Z. Jiang, X. Zhou, C. S. Lee, H. Zhao and W. Zhang, *Adv Mater*, 2018, DOI: 10.1002/adma.201803144, e1803144.
34. J. Huang, S. Wen, G. Chen, W. Chen, G. Wang, H. Fan, D. Chen, C. Song, M. Li, X. Wang, L. Li, M. Tao, B. Li, X. Wang and K. Ostrikov, *Applied Catalysis B: Environmental*, 2020, **277**, 119220.
35. T. Kou, S. Wang, R. Shi, T. Zhang, S. Chiovoloni, J. Q. Lu, W. Chen, M. A. Worsley, B. C. Wood, S. E. Baker, E. B. Duoss, R. Wu, C. Zhu and Y. Li, *Advanced Energy Materials*, 2020, **10**, 2002955.
36. Y. P. Zhu, T. Y. Ma, M. Jaroniec and S. Z. Qiao, *Angew Chem Int Ed Engl*, 2017, **56**, 1324-1328.
37. C. Hu, L. Zhang, Z. J. Zhao, A. Li, X. Chang and J. Gong, *Adv Mater*, 2018, **30**, e1705538.
38. Y.-C. Cao, X. Wu and K. Scott, *International Journal of Hydrogen Energy*, 2012, **37**, 9524-9528.
39. L. A. Diaz, J. Hnát, N. Heredia, M. M. Bruno, F. A. Viva, M. Paidar, H. R. Corti, K. Bouzek and G. C. Abuin, *Journal of Power Sources*, 2016, **312**, 128-136.
40. L. A. Diaz, R. E. Coppola, G. C. Abuin, R. Escudero-Cid, D. Herranz and P. Ocón, *Journal of Membrane Science*, 2017, **535**, 45-55.
41. M. K. Cho, H.-Y. Park, H. J. Lee, H.-J. Kim, A. Lim, D. Henkensmeier, S. J. Yoo, J. Y. Kim, S. Y. Lee, H. S. Park and J. H. Jang, *Journal of Power Sources*, 2018, **382**, 22-29.
42. I. Vincent, A. Kruger and D. Bessarabov, *International Journal of Hydrogen Energy*, 2017, **42**, 10752-10761.
43. H. Ito, N. Kawaguchi, S. Someya, T. Munakata, N. Miyazaki, M. Ishida and A. Nakano, *International Journal of Hydrogen Energy*, 2018, **43**, 17030-17039.
44. M. K. Cho, H.-Y. Park, S. Choe, S. J. Yoo, J. Y. Kim, H.-J. Kim, D. Henkensmeier, S. Y. Lee, Y.-E. Sung, H. S. Park and J. H. Jang, *Journal of Power Sources*, 2017, **347**, 283-290.
45. Y. Leng, G. Chen, A. J. Mendoza, T. B. Tighe, M. A. Hickner and C. Y. Wang, *J Am Chem Soc*, 2012, **134**, 9054-9057.
46. A. Carbone, S. C. Zignani, I. Gatto, S. Trocino and A. S. Aricò, *International Journal of Hydrogen Energy*, 2020, **45**, 9285-9292.
47. C. Busacca, S. C. Zignani, A. Di Blasi, O. Di Blasi, M. Lo Faro, V. Antonucci and A. S. Aricò, *International Journal of Hydrogen Energy*, 2019, **44**, 20987-20996.
48. A. Konovalova, H. Kim, S. Kim, A. Lim, H. S. Park, M. R. Kraglund, D. Aili, J. H. Jang, H.-J. Kim and D. Henkensmeier, *Journal of Membrane Science*, 2018, **564**, 653-662.
49. D. D. Tham and D. Kim, *Journal of Membrane Science*, 2019, **581**, 139-149.
50. E. J. Park, C. B. Capuano, K. E. Ayers and C. Bae, *Journal of Power Sources*, 2018, **375**, 367-372.
51. Y. S. Park, J. H. Lee, M. J. Jang, J. Jeong, S. M. Park, W.-S. Choi, Y. Kim, J. Yang and S. M. Choi, *International Journal of Hydrogen Energy*, 2020, **45**, 36-45.

52. J. Lee, H. Jung, Y. S. Park, S. Woo, N. Kwon, Y. Xing, S. H. Oh, S. M. Choi, J. W. Han and B. Lim, *Chemical Engineering Journal*, 2021, **420**, 127670.
53. Y. S. Park, M. J. Jang, J. Jeong, S. M. Park, X. Wang, M. H. Seo, S. M. Choi and J. Yang, *ACS Sustainable Chemistry & Engineering*, 2020, **8**, 2344-2349.
54. P. Chen and X. Hu, *Advanced Energy Materials*, 2020, **10**, 2002285.
55. J. Chang, Q. Lv, G. Li, J. Ge, C. Liu and W. Xing, *Applied Catalysis B: Environmental*, 2017, **204**, 486-496.
56. J. Hnát, M. Plevova, R. A. Tufa, J. Zitka, M. Paidar and K. Bouzek, *International Journal of Hydrogen Energy*, 2019, **44**, 17493-17504.
57. P. Thangavel, M. Ha, S. Kumaraguru, A. Meena, A. N. Singh, A. M. Harzandi and K. S. Kim, *Energy & Environmental Science*, 2020, **13**, 3447-3458.
58. T. Pandiarajan, L. John Berchmans and S. Ravichandran, *RSC Advances*, 2015, **5**, 34100-34108.
59. L. Xiao, S. Zhang, J. Pan, C. Yang, M. He, L. Zhuang and J. Lu, *Energy & Environmental Science*, 2012, **5**, 7869.
60. S. Seetharaman, R. Balaji, K. Ramya, K. S. Dhathathreyan and M. Velan, *International Journal of Hydrogen Energy*, 2013, **38**, 14934-14942.
61. D. Aili, M. K. Hansen, R. F. Renzaho, Q. Li, E. Christensen, J. O. Jensen and N. J. Bjerrum, *Journal of Membrane Science*, 2013, **447**, 424-432.
62. L. Wang, T. Weissbach, R. Reissner, A. Ansar, A. S. Gago, S. Holdcroft and K. A. Friedrich, *ACS Applied Energy Materials*, 2019, **2**, 7903-7912.
63. P. Fortin, T. Khoza, X. Cao, S. Y. Martinsen, A. Oyarce Barnett and S. Holdcroft, *Journal of Power Sources*, 2020, **451**, 227814.
64. M. R. Kraglund, M. Carmo, G. Schiller, S. A. Ansar, D. Aili, E. Christensen and J. O. Jensen, *Energy & Environmental Science*, 2019, **12**, 3313-3318.
65. H. J. Park, S. Y. Lee, T. K. Lee, H.-J. Kim and Y. M. Lee, *Journal of Membrane Science*, 2020, **611**, 118355.
66. X. Su, L. Gao, L. Hu, N. A. Qaisrani, X. Yan, W. Zhang, X. Jiang, X. Ruan and G. He, *Journal of Membrane Science*, 2019, **581**, 283-292.
67. R. Iwata, L. Zhang, K. L. Wilke, S. Gong, M. He, B. M. Gallant and E. N. Wang, *Joule*, 2021, **5**, 887-900.
68. X. Wu and K. Scott, *International Journal of Hydrogen Energy*, 2013, **38**, 3123-3129.
69. S. H. Ahn, B.-S. Lee, I. Choi, S. J. Yoo, H.-J. Kim, E. Cho, D. Henkensmeier, S. W. Nam, S.-K. Kim and J. H. Jang, *Applied Catalysis B: Environmental*, 2014, **154-155**, 197-205.
70. A. K. Niaz, A. Akhtar, J.-Y. Park and H.-T. Lim, *Journal of Power Sources*, 2021, **481**, 229093.
71. G. Gupta, K. Scott and M. Mamlouk, *Journal of Power Sources*, 2018, **375**, 387-396.
72. M. S. Cha, J. E. Park, S. Kim, S.-H. Han, S.-H. Shin, S. H. Yang, T.-H. Kim, D. M. Yu, S. So, Y. T. Hong, S. J. Yoon, S.-G. Oh, S. Y. Kang, O.-H. Kim, H. S. Park, B. Bae, Y.-E. Sung, Y.-H. Cho and J. Y. Lee, *Energy & Environmental Science*, 2020, **13**, 3633-3645.
73. X. Yan, X. Yang, X. Su, L. Gao, J. Zhao, L. Hu, M. Di, T. Li, X. Ruan and G. He, *Journal of Power Sources*, 2020, **480**, 228805.
74. M. Bhushan, M. Mani, A. K. Singh, A. B. Panda and V. K. Shahi, *Journal of Materials Chemistry A*, 2020, **8**, 17089-17097.
75. J. Parrondo, C. G. Arges, M. Niedzwiecki, E. B. Anderson, K. E. Ayers and V. Ramani, *RSC Advances*, 2014, **4**.
76. D. Li, E. J. Park, W. Zhu, Q. Shi, Y. Zhou, H. Tian, Y. Lin, A. Serov, B. Zulevi, E. D. Baca, C. Fujimoto,

- H. T. Chung and Y. S. Kim, *Nature Energy*, 2020, **5**, 378-385.
77. R. Soni, S. Miyanishi, H. Kuroki and T. Yamaguchi, *ACS Applied Energy Materials*, 2020, **4**, 1053-1058.
78. J. Xiao, A. M. Oliveira, L. Wang, Y. Zhao, T. Wang, J. Wang, B. P. Setzler and Y. Yan, *ACS Catalysis*, 2020, **11**, 264-270.
79. F. Razmjooei, T. Morawietz, E. Taghizadeh, E. Hadjixenophontos, L. Mues, M. Gerle, B. D. Wood, C. Harms, A. S. Gago, S. A. Ansar and K. A. Friedrich, *Joule*, 2021, **5**, 1776-1799.
80. G. A. Lindquist, S. Z. Oener, R. Krivina, A. R. Motz, A. Keane, C. Capuano, K. E. Ayers and S. W. Boettcher, *ACS Appl Mater Interfaces*, 2021, DOI: 10.1021/acsami.1c06053.